CORROSION
The Journal of Science and Engineering

The Role of Nickel in Low Alloy Steels exposed to H2S containing environments. Part I: Trench Formation at the Open Circuit Potential

Journal:	*CORROSION*
Manuscript ID	CJ-2308-OA-4436
Manuscript Type:	Original Article
Date Submitted by the Author:	30-Aug-2023
Complete List of Authors:	Chalfoun, Dannisa R.; Instituto Jorge A Sabato Kappes, Mariano; Comision Nacional de Energia Atomica, Perez, Teresa; Otegui, José ; CONICET La Plata Iannuzzi, Mariano; Curtin University, WASM:MECE; Norges teknisk-naturvitenskapelige universitet, Department of Engineering Design and Materials
Key Words:	steel, sulfide stress cracking, slow strain rate tests, open-circuit potential, hydrogen sulfide , hydrogen embrittlement, cracking

The Role of Nickel in Low Alloy Steels exposed to H_2S-containing environments. Part I: Trench Formation at the Open Circuit Potential

Dannisa R. Chalfoun,,** Mariano A. Kappes,‡, *,**,*** Teresa E. Perez,** José L. Otegui,*** and Mariano Iannuzzi,****

‡Corresponding author. E-mail: kappes@cnea.gov.ar

*Comisión Nacional de Energía Atómica (CNEA), Av. General Paz 1499, San Martín, Buenos Aires, B1650KNA, Argentina

**Instituto Sabato, Universidad de San Martín (UNSAM) – CNEA, Av. General Paz 1499, San Martín, Buenos Aires, B1650KNA, Argentina

***Consejo Nacional de Investigaciones Científicas y Técnicas (CONICET), Godoy Cruz 2290, Ciudad Autónoma de Buenos Aires, C1425FQB, Argentina

****Alcoa of Australia, PO BOX 252, Applecross, Western Australia, 6953, Australia

ABSTRACT

The nickel content in low alloy steels (LAS) for oil and gas exploration and production is limited to a maximum of 1 wt.% according to ANSI/NACE MR 0175/ ISO 15156. This restriction is imposed to avoid sulfide stress cracking (SSC) in sour (H_2S-containing) environments. In this work, the effect of Ni on SSC of LAS was studied independently of other alloying elements. For this purpose, quenched and tempered steels heat treated to a yield strength of 610 MPa with a Ni content below and above the 1 wt.% threshold were evaluated at the open circuit potential (OCP) in unstressed specimens, and in slow strain rate tests (SSRT) at room temperature. Thiosulfate was used as a surrogate of H_2S, according to the Tsujikawa method. It is concluded that Ni contributes to the stabilization of the sulfide films that form on the steel's surface at OCP. The rupture of this film due to tensile stress promotes the nucleation of elongated deep pits, referred to as trenches, which can act as sulfide stress crack initiators. Trenches were observed exclusively in stressed, Ni-containing specimens. Moreover, trenches' morphology, dimensions, and distribution varied with the Ni content in the steels. For the steels studied in this work, the Ni effect on trenching persisted below the 1 wt.% threshold.

KEYWORDS: *Low Alloy Steels, Sulfide Stress Cracking, Nickel, H_2S, Environmental Assisted Cracking, hydrogen, trenches, thiosulfate*

1 INTRODUCTION

The first records of failures due to Sulfide Stress Cracking (SSC) of Oil Country Tubular Goods (OCTG) operating in H_2S-containing oil and gas (O&G) wells date from 1952.[1,2] These predominantly intergranular failures occurred in the inner side and the external wall, of 9 wt.% Ni steel tubing and casing components after a relatively short time in service.[1,2] In all cases, the steels had a yield strength (YS) above 552 MPa (80 ksi) and a moderate corrosion rate of 0.254 mm/y (10 mils/y).[1] Failures were not exclusively associated with Ni. In this regard, Cr-containing and Mn-Mo containing steels evidenced cracking, too.[2] The possible correlation between the SSC susceptibility of the steels and their chemical composition and microstructural characteristics was studied by Fraser et al. by means of statistical analysis using three-point bending tests (TPBT) on 104 different steel compositions including commercial grades.[3] Fraser et al. established that high levels of hardness and mechanical strength, as well as a high content of nickel, molybdenum, or both could be detrimental to the resistance of steels to SSC.[3,4] The effect of Ni in steels was investigated by Treseder and Swanson using normalized and quenched and tempered (Q&T) AISI 4340 (1.65 – 2 wt.% Ni) and AISI 4140 (< 0.25 wt.% Ni) steels.[5] Treseder and Swanson compared the critical stress (Sc), an artificial value to quantify the cracking resistance of different materials, calculated after

TPBT with field experience data and arrived to the relationship of Sc ≥ 10 psi x 10^{-4} for an SSC resistant steel.[5] Sc was obtained statistically from the measured deflections of the beams and represented the critical stress at which the probability of failure was equal to 50% after 720 h of exposure to a 0.5% acetic acid solution saturated with H_2S at 101.3 kPa in TPBT at 21°C.[5,6] Steels with a Ni content above 1 wt.% and a hardness greater than 22 HRC (235 HBN) presented values of Sc between 1.75 and 4.8.[5] AISI 4140 steels with HRC < 22 had Sc values between 11 and 15, while the values of Sc for Ni-containing AISI 4340 steels with a HRC < 22 were around 3 to 9.[5] Treseder and Swanson results were foundational to establish the requirements in ANSI(1)/NACE(2) MR0175/ISO(3) 15156 standard for SSC resistant materials selection for O&G exploration and production. Particularly, for carbon steels and LAS, the maximum hardness is limited to 22 HRC and the Ni content to a maximum of 1 wt.%.[7,8] Steels must be in an annealed, or normalized, or normalized and tempered, or quenched and tempered condition.[7,8] These requirements are part of the Option 1 in the current version of ISO 15156-2 for the qualification and selection of carbon steels and LAS with resistance to SSC, stress-oriented hydrogen-induced cracking (SOHIC), and soft-zone cracking (SZC) for partial pressures of H_2S higher than 0.3 kPa.[8]

Sc is normally used to rank quantitatively the SSC resistance of different steels and it cannot be used as a design or operating parameter.[5,6] In a discussion section included in Treseder and Swanson's paper, Snape criticized the obtained results arguing that the criterion of Sc = 10 for SSC resistant steels was supported by limited field data.[5] Additionally, Snape emphasized that the authors[5] ignored the presence of two drill holes of 1 mm in diameter in the center of the test specimens that acted as stress concentrators, raising the local stress well above the YS of the steels.[5] Hence, Snape argued that Sc obtained using drilled specimens is unrelatable to allowable stresses in service condition.[5] With regard to the metallurgy of the evaluated steels, Snape suggested that comparisons must be made between steels with the same microstructure.[5] Snape also suggested that the unsatisfactory performance of the Q&T Ni-containing steels could be due to the presence of detrimental phases in the microstructure instead of the nickel content *per se*.[5] Snape argued that an increase in Ni decreases the lower critical temperature (Ac1) in the steels. In this regard, austenite formation occurs if Ac1 is exceeded during tempering, which could transform to untempered martensite upon cooling.[5] The Ni-containing steels studied by Treseder and Swanson had also Cr and Mo. These elements confer strength by second phase hardening and therefore higher tempering temperatures are required to decrease the hardness below 22 HRC.[5] Cautious tempering below Ac1 was performed by Snape in Ni-containing steels, resulting in an increase in SSC resistance obtained using the same TPBT method.[5] According to Snape, this was related to the absence of fresh martensite after the first quenching and tempering cycle under controlled conditions of time and temperature.[5] The corollary of Snape's discussion to Treseder and Swanson's results is that the SSC performance of steels cannot be assessed exclusively by hardness and chemical composition.[5] The implication is that the microstructure of the steel should also be considered.

Except for S, which forms non-metallic inclusions with Mn that could favor crack initiation, and for P, an impurity with a great tendency to segregate to grain boundaries promoting the formation of hard spots with low toughness, the effect of alloying elements on the SSC susceptibility of LAS is still debated by the international materials community.[9,10] Furthermore, as the severity of the environment increases, the mechanical strength of the steels plays a paramount role since an increase in the YS beyond 690 MPa (100 ksi) drastically reduces the SSC resistance.[11,12] Nonetheless, a microstructure optimization-based paradigm was developed by steel manufacturers in search of high-strength LAS which are resistant to SSC.[13–17] The key factors in obtaining SSC resistant microstructures lie in the correct design of the heat treatment parameters considering the chemical composition of the steels to avoid the presence of undesired hard phases and, also in the control of the cleanliness of the

(1) American National Standards Institute (ANSI) 1899 L St. N.W., Washington, DC 20036, USA
(2) National Association of Corrosion Engineers (NACE) 15835 Park Ten Place, Houston, Texas 77084, USA
(3) International Organization for Standardization (ISO) Chemin de Blandonnet 8 CP 401 1214 Vernier, Geneva, Switzerland

steels to ensure a low level of inclusions.[13] Additionally, cold work and other processes that can impart tensile residual stresses should be minimized and/or preventive measures, such as stress relief operations, should be taken to avoid the negative effect on SSC resistance. Several authors agree that LAS containing a fully tempered martensite microstructure, i.e., fine and spheroidized carbides uniformly distributed in a refined grain ferrite matrix, have the greatest SSC resistance at a given strength level when compared to ferritic-pearlitic and bainitic containing microstructures.[9,13,14,18]

Adding Ni to LASs is desirable because it increases hardenability and fracture toughness and decreases the ductile-brittle transition temperature.[19–21] Hence, Ni as an alloying element favors uniform Q&T microstructures, with the greatest SSC resistance, even across thick-wall components for extreme environments (e.g., high pressure and high/low temperature). From this perspective, the restriction in ISO 15156 on an alloying element that favors transformation to the most resistant microstructure to SSC is paradoxical. The so called "Ni effect" in the SSC susceptibility of commercial grades of LAS and Ni-containing laboratory Cr-Mo steels at different microstructural conditions was evaluated by many authors without reaching a conclusive result.[14,22–31] On one side, the effect of Ni on SSC is comprised of interplaying factors related to the control of microstructure during heat treatment and the resulting mechanical properties. Those factors could have different effects in SSC resistance, which involves resistance to crack initiation and resistance to crack propagation. The material resistance to crack propagation in sulfide environments is often measured by fracture mechanics approaches that use precracked specimens exposed at constant displacement in an H_2S-containing environment.[6,32] From those tests, the value of the critical stress intensity factor for crack arrest in the H_2S environment (K_{ISSC}), i.e., the environment affected fracture toughness, can be estimated. For homogeneous, properly Q&T microstructures without untempered martensite, at a given strength level, no detrimental effect of up to 5 wt.% Ni was apparent, considering K_{ISSC} values.[23–25,31] Hence, these results suggest that the postulated negative nickel effect in SSC is related to non-optimized heat treatments or an effect in SSC initiation. Certainly, for a given steel chemistry, the K_{ISSC} value is dependent on material strength and microstructure, and few degrees difference in tempering temperature can have a great impact on its microstructure and K_{ISSC} values. This can be illustrated by the results reported by Payer, where 2.11 wt.% Ni steels quenched and tempered at temperatures 16°C below Ac1 showed a decrease of 35% in K_{ISSC} compared with the values obtained for a quenching and tempering at 29 °C below Ac1 (20 vs. 27 $MPa.m^{-1/2}$).[24] Additionally, a remarkable improvement in K_{ISSC} was obtained after a second tempering treatment for that steel (32 $MPa.m^{-1/2}$).[24] Regarding the Ni addition to LAS, Payer observed that commercial quenched and double tempered steels with 2.85 wt.% Ni (YS = 698 MPa) had K_{ISSC} values similar to those of nickel-free steels with a YS = 649 MPa and tempered martensite microstructure (40 $MPa.m^{-1/2}$).[24] Based on these results, regardless of the Ni content, an adequate resistance to SSC crack propagation in H_2S-containing environments can be achieved with a careful microstructure control.

Crack initiation in sulfide environments commonly occurs at stress-concentrating points. Corrosion pits or inclusions discontinuities are common stress concentrators in laboratory tests performed on finely grounded specimens. Tests with smooth specimens, subjected to constant or increasing load or strain, are suitable for determining resistance to crack initiation. For tests at constant load or constant strain, the output of the tests is time to failure, which is affected by both resistance to crack initiation and resistance to crack propagation. The so called "threshold stress" is the maximum stress level below which no cracks are present in specimens stressed for 30 days.[6] Many authors noted that despite a meticulous microstructure control, the SSC threshold stress (σ_{th}) is reduced with increased Ni content in steels with similar YS.[24,30,31] For example, after constant load tests according to Method A of the NACE TM 0177 standard, a 1.8 wt.% Ni-containing steel (YS = 828 MPa), quenched and tempered at 600°C, had a σ_{th} = 164 MPa, which was almost four times lower than that of a Ni-free steel (YS = 808 MPa) with the same base chemical composition and heat treatment.[31] The effect was associated with the formation of trenches on the gauge length of the specimens after exposure

to a NACE TM0177 solution A (5 wt.% NaCl and 0.5 wt.% glacial acetic acid) saturated with H_2S at 101.3 kPa at the open circuit potential (OCP) at room temperature.[30,31] Trenches are elongated deep pits considered as a transitional morphology between pitting and cracking.[30] While several authors associated trenches to the presence of nickel,[4,25,26,31,33] these features were also reported after testing Cr-Mo steels without Ni[23,24,30,34,35]. While many authors have concluded that trenches act as SSC initiation sites, the role of Ni on trench formation has still not been clearly elucidated.

The purpose of this work was to study the effect of nickel content on SSC resistance of Q&T LASs independently from other alloying elements. For this purpose, steels with a simple chemical composition and with varying Ni contents were manufactured where carbide former elements like Cr, Mo, and V were not included. The electrochemical behavior of the Ni-containing steels was studied with and without applied tensile loads in a simulated sour environment by adding controlled amounts of sodium thiosulfate to a NACE TM0177 solution A as in Tsujikawa Method.[36–39] This is the first part of a publication where the Ni effect at OCP is presented. In the second part manuscript, tests were performed at potentials above and below the OCP to explore the origins and nature of the trench formation mechanism.

2 EXPERIMENTAL PROCEDURES

The experimental matrix was designed to analyze the effect of Ni on the electrochemical behavior of LASs in non-stressed specimens and in SSRT tests conducted at the OCP at room temperature.

2.1 Materials and Heat Treatment

Five 45 kg carbon steel ingots with varying nickel content were obtained by vacuum induction melting and subsequently forged and hot-rolled to obtain plates of a nominal thickness of 10 mm. The nickel content was varied between 0 and 5 wt.%, in a carbon steel with a simple chemical composition as indicated in Table 1.[40] The addition of C, Mn, and Si conferred sufficient hardenability to obtain a fully quenched microstructure when the 10 mm square bars were quenched in an iced brine bath. From those bars, specimens for all tests could then be machined. Sulfur and phosphorus contents were limited to maximum levels of 0.0010 wt.% and 0.0006 wt.%, respectively, to minimize the presence of detrimental inclusions in the steels, and to prevent temper embrittlement, caused by the segregation of impurities to grain boundaries during prolonged exposure to temperatures between 350°C and 550°C. The propensity of impurity segregation is reduced when the J factor (or Watanabe factor) (Equation 1) is below 100. On the other side, the X factor (or Bruscato factor) weighs the level of impurities on the susceptibility to temper embrittlement (Equation 2). A steel is considered immune to temper embrittlement if X < 15. The input values of the elements to calculate the J factor must be expressed in wt.%, and in ppm for the X factor. For the steels studied 7 < J < 10 and 0.4 < X < 0.7.[41,42]

$$J = (Mn + Si)(P + Sn) \times 10^4 \qquad (1)$$

$$X = (10\,P + 5\,Sb + 4\,Sn + As) \times 10^{-2} \qquad (2)$$

Specimens were normalized and Q&T to obtain a microstructure consisting of approximately 100% tempered martensite, independently of Ni content. The decrease of Ac1 with Ni content was previously quantified with differential scanning calorimetry to avoid exceeding it during the tempering.[40] The target hardness after tempering was close but still below 22 HRC, and the tempering temperature was selected after preliminary treatments conducted at several temperatures in the range from 500 to 600 °C [40]. Steels with 0, 0.5, 1 and 3 wt.% Ni were tempered for 1 h at 550°C while the tempering temperature for the 5 wt.% Ni steel was 575°C. Tensile tests in air, through-thickness Rockwell C hardness (HRC)

measurements of as quenched and Q&T microstructures, and a metallographic characterization were conducted. Similar mechanical properties (Table 1) and a homogeneous Q&T martensitic microstructure (Figure 1) were obtained after performing the heat treatments.[40] HRC surface measurements were used as a rapid control of the heat treatment effectiveness for each test specimen. All the heat-treated alloys had a hardness level below but near the 22 HRC threshold established by ISO 15156-2 standard. The steel without nickel and with and 0.5 wt.% Ni had a hardness below 20 HRC, the lowest level measurable on this scale. Prior austenitic grain size (PAGS) was measured according to the interception method in ASTM E 112.[43] A slight decrease of the PAGS was observed with the increase in Ni content in the steels as indicated in Table 1.

2.2 Testing Environment

The tests were conducted in a deaerated NACE TM0177 solution A (5 wt.% NaCl and 0.5 wt.% glacial acetic acid), referred to as NACE solution A hereafter at a pH between 2.7 and 2.8, at room temperature and 101.3 kPa total pressure.[6] In all cases, the H_2S bubbling was substituted by adding sodium thiosulfate ($Na_2S_2O_3$) to simulate an H_2S-containing environment. This alternative was proposed by Tsujikawa et al. for SSC testing of LASs and corrosion-resistant alloys.[36] Laboratory tests with thiosulfate are simpler than conventional gaseous H_2S evaluations because sodium thiosulfate is an innocuous salt. According to Tsujikawa, in acid environments and at the corrosion potentials of LASs, thiosulfate reduces to H_2S, generating this gas locally on the surface of the metal. Based on previous results, the optimum concentration of thiosulfate as a substitute of H_2S in NACE solution A is 10^{-3} M.[36,37,39] At a higher concentration the corrosion rate increases with a decrease in the amount of absorbed hydrogen.[37–39] Kappes et al. determined that the effective H_2S concentration in the vicinity of a carbon steel electrode's surface at a concentration of 10^{-3} M $S_2O_3^{2-}$ in NACE solution A is equivalent to that obtained in the same solution saturated with a partial pressure of 0.56 kPa H_2S in N_2.[39] Additionally, Tsujikawa reported that the ductility loss in a SSRT due to SSC in a 10^{-3} M $S_2O_3^{2-}$ substituted NACE solution A was similar to that obtained in artificial seawater saturated with H_2S at 101.3 kPa.[36]

All the tests reported in this work were conducted in a 10^{-3} M $S_2O_3^{2-}$ substituted NACE solution A, which was prepared by adding 5 mL of a fresh 0.2 M $Na_2S_2O_3$ solution per liter. Special considerations were taken to avoid potential contamination of the electrolyte with oxygen. Firstly, the solution and the testing cell were deaerated with N_2 bubbling before thiosulfate was added to the solution. After adding thiosulfate to the deaerated solution, it was transferred to the cell, where the steel electrode was already placed, and the corresponding test was started. Additionally, for measuring polarization curves, the counter electrode (CE) was placed in a bridge tube that allowed ionic conduction through a fritted glass tip but avoided the contamination of the test solution with products of the reactions occurring at the surface of the CE.

2.3 Electrochemical Tests

Specimens were cut from the steel plates and ground with SiC emery paper up to 600 grit. The specimens were coated with epoxy resin, leaving an area of 1.5 cm^2 of the plane containing the rolling and transverse directions exposed to the solution. A five-port glass cell with N_2 deaeration capabilities was used. The steel specimen was immersed in the solution once it was deaerated. The potential was measured *versus* a KCl saturated calomel reference electrode (SCE) and a graphite bar served as a counter electrode. For safety reasons, the gas exiting the cell was passed through a trap containing 0.1 M NaOH to neutralize and capture the H_2S formed during the thiosulfate reduction.

OCP evolution was measured for 72 h in a deaerated NACE solution A containing 10^{-3} M $S_2O_3^{2-}$, at ambient temperature, to allow the formation of a sulfide film on the exposed area. The nature of the films formed in 0 and 5 wt.% Ni LASs was analyzed by grazing incidence X-ray diffraction (XRD) at an angle of 1° and a 0.02° step, using a multipurpose diffractometer with Cu radiation. Subsequently, the sulfide film was

removed from each specimen by a 30 s immersion in an inhibited HCl solution, containing 2 g of antimony trioxide and 50 g of stannous chloride per liter of HCl.[44] Scanning electron microscopy (SEM) was used to analyze the morphology of the surface before and after the sulfide film removal. Blank tests (i.e., specimens polished to 600 grit and subsequently immersed for 30 s in the inhibited HCl solution) were also observed under SEM and there were no signs of corrosion on the surface of those blank specimens, regardless of the Ni content. OCP evolution measurement for 72 h was also conducted in a deaerated NACE solution A without thiosulfate additions.

To analyze the effect of nickel on the electrochemical behavior of each steel, anodic and cathodic potentiodynamic polarization curves were obtained in deaerated NACE solution A containing 10^{-3} M $S_2O_3^{2-}$ at ambient temperature. The OCP was measured for 24 h before polarizing the electrode. A scan rate of 0.167 mV/s was used. For each experimental condition, all the tests were conducted in duplicate.

2.4 Slow Strain Rate Tests

Slow strain rate tests (SSRTs) were conducted at room temperature to evaluate the SSC susceptibility of the steels at the OCP as a function of nickel content. Cylindrical specimens with threaded ends were machined from the plates with the axis parallel to the rolling direction of the plates. The bars were heat-treated to produce a Q&T microstructure (Figure 1) with mechanical properties as detailed in Table 1. The gauge diameter and length were 3.81 mm and 25.4 mm, respectively, and machining was conducted following the recommendations in NACE TM0198.[45] The gauge section was polished with SiC emery paper up to 4000 grit to obtain an average roughness below 0.25 µm as required in the standard.[45] Specimens were threaded in the pull rods. For tests in NACE solution A, an epoxy coating was applied to the shoulders of the specimens and the pull rods, leaving only the gauge length uncoated and, thus, avoiding undesired galvanic effects. The strain rate was set to 10^{-6} s^{-1} resulting in a crosshead displacement speed of 2.54 x 10^{-5} $mm.s^{-1}$. The selected strain rate value was sufficiently low to allow the occurrence of corrosion reactions and hydrogen diffusion required to evaluate an environmental-assisted cracking phenomena.[46,47] Additionally, tensile tests were performed in air in specimens of the same size for comparison. For the tests in air, a crosshead displacement speed of 8.33 x 10^{-4} mm. s^{-1} was used until the YS was reached. At this point, the extensometer was removed, and the test was continued at a crosshead speed of 0.0167 mm. s^{-1}. Stress-strain curves were corrected to eliminate the contribution of the compliance of the tensile-test machine in the elastic regime.

Considering the exposed steel area and the expected duration of the SSRT, a 3.5 L poly (methyl methacrylate) cell was specially constructed for containing the testing solution. The large capacity of the cell ensured a solution volume to exposed steel area ratio of 0.544 L/cm^2 that prevented the depletion of thiosulfate during the tests.[39] The cell had five ports for the working electrode, counter electrode (for tests under electrochemical polarization to be reported in Part II of this work), reference electrode, and N_2 inlet/outlet. The N_2 outlet was connected to a 0.1 M NaOH trap to neutralize the H_2S produced on the steel surface as a consequence of the thiosulfate reduction reaction.

A preconditioning stage before starting each SSRT allowed for reaching the hydrogen saturation of the specimen and the formation of a black sulfide film on the exposed metallic surface at OCP. For a cylindrical specimen, the time required to reach a homogeneous hydrogen distribution along the specimen radius can be approximated from a solution to Fick's second law in cylindrical coordinates as proposed by Crank.[48] The H concentration in the center of the specimen is higher than 95% of the surface H concentration when $D.t/r^2 > 0.6$, where D is the diffusion coefficient, t is pre-charging time and r is the radius of the cylinder.[48] In a previous work by the same authors of this paper, a decrease in the apparent hydrogen diffusion coefficient (D_{app}) was obtained as Ni was incorporated into the steels.[49] The lowest D_{app}, corresponding to the steel containing 5 wt.% Ni at room temperature, was selected for a conservative estimation of the required time to have a H saturation in the center of

the 3.81 mm diameter tensile bar. Thus, setting r = 1,9 mm, a charging time of 2.7 h was obtained using $D_{app,5Ni\text{-}steel}$ = 2.3 x 10^{-6} $cm^2.s^{-1}$.[49] It must be noted that the D_{app} is lower than the lattice diffusion coefficient of annealed iron (D_l = 7.6 x 10^{-5} $cm^2.s^{-1}$) because it considers the presence of hydrogen traps in the steel microstructure. Additionally, after 24 h at the OCP the exposed surface was covered with a black sulfide film. Given the above considerations, the preconditioning period at OCP before SSRT was set to 24 h for all specimens.

2.5 Loss of Ductility and Specimens Examination after SSRTs

The cracking susceptibility of the specimens was estimated using the plastic elongation ratio parameter (RE) (Equation 3) and the reduction of area ratio (RRA) (Equation 4):[47]

$$RE = E_e/E_c \quad (3)$$

where E_e is the plastic elongation in the corrosive environment and E_c corresponds to that in the control environment (air).[47]

$$RRA = RA_e/RA_c \quad (4)$$

where RA_e is the reduction in area measured after fracture of the specimens in the corrosive environment and RA_e corresponds to that in the control environment (air).[47] The susceptibility to SSC increases with a decrease in RE and RRA, and a value close to 1 would indicate similar ductility in the environment vs. air.

The presence of secondary cracks along the gauge length was evaluated by SEM and light optical microscopy analysis of longitudinal cross-sections. SSC susceptibility was also characterized qualitatively according to the morphology of trenches and secondary cracks on the gauge length. Those features were also quantitatively analyzed by measuring the average density, depth (d), width (a), and the aspect ratio (d/a) on optical micrographs of cross sections under high contrast at 10X with a software (ImageJ). For this purpose, a baseline was defined on each micrograph from which the depth was determined. The width was measured at the trench mouth. These parameters were evaluated for all the indications in the micrograph at 10X and an average value was obtained for each of them. The aspect ratio was calculated as d/a. The average density was calculated as the number of secondary indications present per total length (in mm) of the micrograph at 10X.

3 RESULTS

3.1 Open Circuit Potential Evolution during 72 h

The OCP increased with time and a stable value was reached after a few hours of exposure to the 10^{-3} M $S_2O_3^{2-}$ substituted NACE solution A. Thereafter, potential variations were small (less than 10 mV) until completing the 72 h test duration, Figure 2. The time required to reach a stable potential decreased for steels with higher Ni contents. Additionally, the increase in Ni in the steel shifted the OCP to more noble values. Initial OCP values for 0, 1, and 5 wt.% Ni steels were – 679, – 657, and – 589 mV_{SCE}, correspondingly and after 10 h, 5 h, and 2.5 h, reached a stable potential of – 653, – 587, and – 535 mV_{SCE}, respectively. Duplicate tests showed deviations in OCP approximately 10 mV or lower. The initial solution pH was between 2.7 and 3.0 and pH variations were less than 0.3 at the end of the OCP evolution tests. The measured pH-potentials values measured after 72 h were located in the $S_2O_3^{2-}$ - H_2O Pourbaix diagram at 298 K and 101.3 kPa (Figure 3) calculated in this work according to the reactions detailed in Appendix 1. Regardless of the increase in OCP with Ni content, all the potentials were within the stability field of H_2S and

below the reversible potential for the hydrogen evolution reaction (HER). From a thermodynamics perspective, these results validated using thiosulfate as an alternative to H_2S bubbling[36] for all the alloys studied in this work.

A black corrosion product film covered the original bare surface of all the steels after 24 h of immersion. The film was more compact and adhered to the steel's surface better as the Ni content increased (Figure 4). The nature of these films was analyzed by XRD with grazing incidence, an adequate characterization technique for thin layers.[50] Iron sulfides phases such as cubic FeS and $Fe_{(1-x)}S$ pyrrhotite were identified in the Ni-free steel and the 5 wt.% Ni steel (Figure 5). Additionally, nickel sulfide (Ni_3S_2) was also detected in the corrosion products layer of the Ni-containing steel. In both steels, cementite (Fe_3C) was found after 72 h of exposure to the thiosulfate solution, suggesting a preferential corrosion of the ferrite, in accordance with previous studies [37]. In all cases, the baseline of the diffractograms was corrected by subtracting the background and eliminating the curvature of the diffracted beam at low diffraction angles (2θ) due to the low angle of incidence used (i.e., 1°). Removing the background could have eliminated information on the presence of amorphous phases, e.g., amorphous FeS. This phase is not expected to give an XRD pattern but can be evidenced as a wide peak at 16.5°.[51,52] In the NACE solution A without thiosulfate, only light-gray and poorly attached corrosion products were present after 72 h of exposure. These layers were easily detached during cleaning of the specimens post-testing, and it was not possible to evaluate them by XRD. After removing the sulfide film with inhibited HCl, the Ni-free steel had an irregular surface with a morphology consistent with uniform corrosion due to general dissolution while the steels with higher nickel content evidenced uneven general corrosion (Figure 4). Shallow pits of 15 µm of diameter were observed on the surface of the specimen with 5 wt.% Ni. All the specimens were free from features such as fissures or deep and elongated pits.

3.2 Cathodic and Anodic Behavior

The analysis of the anodic and cathodic polarization curves showed that Ni had a pronounced effect on the potentials, especially close to the OCP (Figure 6). Nickel retarded the anodic reaction kinetics. For a given potential, for example, at -520 mV_{SCE}, the specimens with 3 and 5 wt.% Ni presented current densities that were an order of magnitude lower (0.48 to 0.23 mA/cm^2, respectively) than for 0, 0.5, and 1 wt.% Ni (4.5 to 2.5 mA/cm^2), Figure 6 a). An opposite effect was observed in the cathodic polarization curves, were Ni promoted the kinetics of the cathodic reactions, Figure 6 b). However, for sufficiently high cathodic or anodic applied potentials, all the curves converged to the same value of current density irrespective of the Ni content of the steel.

3.2.1 Anodic Polarization

Anodic potentiodynamic polarization curves for the steels with 0, 1, and 5 wt.% Ni are indicated in Figure 6 a). These curves were obtained after 24 h of exposure to the substituted NACE solution A. The corrosion potential measured from the polarization curves (E_{corr}) increased with Ni content, while the corrosion current density (i_{corr}) was similar for all the specimens. The i_{corr} values were obtained by extrapolation of the fit lines of the cathodic and anodic branches in the vicinity of the E_{corr}. Regardless of the nickel content in the steels, the i_{corr} values were between 0.04 mA/cm^2 and 0.06 mA/cm^2. In the thiosulfate-containing NACE solution A, the electrochemical behavior was controlled by charge transfer in the vicinity of the corrosion potential close to +50 mV and a diffusion-controlled region was observed for nobler potentials, irrespective of the nickel content of the steels. The diffusion-controlled region is in accordance with the formation of a pseudo-protective sulfide film. At potentials close to -400 mV_{SCE}, all the steels attained the same value of limiting current density (10 mA/cm^2).

3.2.2 Cathodic Polarization

Figure 6 b) shows cathodic potentiodynamic polarization curves for all the steels studied. Those curves were obtained by scanning the potential in the active direction after a previous exposure of 24 h at the OCP in the H_2S simulated solution. This preexposure stabilized the sulfide film in all cases. Independently of the Ni content, two zones were identified in the curves. Initially, the logarithm of the current density increased linearly with the cathodic potential, suggesting charge-transfer control. In this first zone, extending down to -200 mV vs. OCP, the Tafel slope of the curves were -113.2, -103.7, -117.3, -123.3, and -120.3 mV/decade for the steels with 0, 0.5, 1, 3 and 5 wt.% Ni, respectively. These values of Tafel slope are close to 118 mV/decade, i.e., the expected slope for the hydrogen evolution reaction in acid environment[37]. Additionally, thiosulfate may undergo reduction reactions, to elemental sulfur and hydrogen sulfide.[37] The presence of Ni in the steels increased the rate of the cathodic reactions (namely, the exchange current density), as also observed by other authors[23].

The subsequent polarization to potentials more active than -200 mV vs. OCP gave place to a second stage where a limiting cathodic current density between 10 and 30 mA/cm^2 was attained. This behavior is characteristic of an electrochemical diffusion-controlled process.[37] The diffusion-limited current density increased with Ni content. Considering previous work[37], where cathodic polarization curves of a LAS were measured in NACE solution A with and without different additions of thiosulfate, it is likely that the main cathodic reaction in this diffusion-controlled region is the acetic acid reduction reaction.

3.3 Tensile Tests in Air and Slow Strain Rate Testing at OCP

Stress-strain curves obtained for all the steels in air and in the 10^{-3} M $S_2O_3^{2-}$ substituted NACE solution A at OCP are shown in Figure 7. In air, all the steels evidenced a similar degree of plastic elongation, E_c, between 0.23 and 0.26 (Table 1). The reduction in area in air, RA_c, was approximately 84% for all the steels studied (Table 1). The YS was 610 MPa on average for all the steels except for the 3 wt.% Ni steel which had a YS of 630 MPa. The slight increase in the YS of the 3 wt.% Ni steel was attributed to Ni's solid solution strengthening[53]. It is also important to note that the 5 wt.% Ni steel was tempered at a slightly higher temperature (575°C versus 550°C for the other steels). This difference may have offset the Ni solid solution hardening effect. The tensile strength (σ_{UTS}) was close to 740 MPa for the steels with 3 wt.% and 5 wt.% Ni. For the rest of the alloys, σ_{UTS} was between 696 and 708 MPa. After SSRT in the sour brines, no changes in the YS were observed. However, the stress-strain curves indicated that all the steels (including the Ni-free steel) suffered a substantial reduction in plastic elongation compared with air. All specimens failed before reaching the respective σ_{UTS} measured in air.

Figure 8 summarizes the effect of nickel content in SSC susceptibility, with RE and RRA calculated according to Equations 3 and 4. Both parameters followed a similar trend, but RRA presented lower dispersion than RE. Thus, RRA was used to analyze the loss of ductility in this work. The highest ductility was presented by the steel without nickel at values of RRA approximately 0.23 and the lowest value was measured for the steel with 3 wt.% Ni (RRA = 0.09). RRA values for the steels containing 0.5 and 1 wt.% Ni corresponded to half of those measured for the 0 wt.% Ni steel. Nonetheless, RRA increased slightly after increasing the Ni content to 5 wt.%.

OCP evolution versus time was monitored during the specimens' preconditioning stage and the SSRT up to the point of final failure (Figure 9). Figure 9 shows the results for the 0, 1, and 3 wt.% Ni steels. The "$OCP_{72\,h}$" curve corresponds to the results shown in Figure 2, added to Figure 9 for comparison. For those steels, the OCP measured during straining (OCP_{SSRT}) increased during the preconditioning stage, following the $OCP_{72\,h}$ curve. Subsequently, the OCP_{SSRT} curve for those steels stabilized to a potential value close to the one measured without loads applied. For the Ni-free steel, the OCP slightly decreased near the point of maximum engineering stress, σ_{UTS}. Necking likely caused a local increase in strain rate, perturbed the film and exposed bare metal causing the decrease in OCP. In contrast, the 1 and 3 wt.% Ni-containing steels presented a sharp

reduction in OCP before reaching the yield stress. As it will be discussed in Section 4 it is postulated that this decrease in potential marked the onset of localized corrosion, revealed as trenches in the Ni-containing steels. The rest of the Ni-containing steels had a behavior similar to the one shown in Figure 9 for the 1 and 3 wt.% Ni steels.

3.4 Characterization of trenches and secondary cracks after SSRTs

Trenches and secondary cracks were observed along the gauge length of the Ni-containing steels. Figure 10 shows portions of the gauge length after SEM imaging. Figure 11 summarizes the results obtained after the quantification of the average density, length (d), width (a), and aspect ratio (d/a) *versus* Ni content, based on the cross-section inspection of the optical micrographs for each steel studied.

The indications present on the gauge length were classified as follows:

(i) Trenches: elongated features with a rounded or triangular tip (blunted tip) that grow perpendicularly to the applied load that had a minimum depth of 30 µm and an aspect ratio of $1 < d/a < 3$. In some cases, a sharp or branched crack evolved at the trench bottom. In such situations, the reported depth corresponds to the sum of the trench and crack depths.

(ii) Microcracks: very fine cracks with $d >> a$ with a maximum depth of 50 µm, normally nucleated on the surface of the polarized specimens at cathodic potentials (lower than OCP). For the rest of the potentials, these features were only observed in the necking area of the evaluated specimens.

(iii) Cracks: sharp—or branched— and elongated cracks nucleated at the bottom of the trenches, that can present a transgranular and/or intergranular pattern. The minimum depth of the cracks measured from the trench tips was 30 to 50 µm. Maximum values of crack depth were around 130 to 400 µm.

The Ni-free specimens evidenced uniform corrosion along the exposed surface to the environment; thus, the measured density of indications was nil. Some isolated pits were observed, but no trenches or secondary cracks were found in the absence of Ni, except for microcracks close to the principal crack after the SSRT, where necking concentrated most of the plastic strain after the point of maximum stress. In contrast, all the Ni-containing steels presented secondary indications on the gauge length even away from the final rupture area. The depth and aspect ratio of trenches and cracks increased with Ni content. The width was almost independent of Ni content, and the density was maximum for the steel with 1 wt.% Ni. It is worth noting that the cross-sections of the 0.5 and 1 wt.% Ni steels were saturated with trenches (Figure 10). This condition was defined in this work as the point where the mean interspacing of trenches was on the order of the average width of the measured defects. Trenches with blunted tips were found on the gauge length of the steels with 0.5 and 1 wt.% Ni. On the other hand, secondary cracks nucleated at the bottom of trenches in the steels with 3 wt.% Ni and 5 wt.% Ni. Among the nickel-containing steels, the 3 and 5 wt.% Ni steels had the lowest density of indications but the largest total depth of cracks (including trench + crack depth). Consequently, the aspect ratio for the 5 wt.% steel was the highest, approximately 7, while d/a was between 1 and 3 for the rest of the Ni-containing steels, Figure 11.

Figure 12 a) shows the cross-sections for the 0.5 wt.% Ni steel, where trenches with a blunted tip predominated. An incipient 10 µm crack nucleated at the tip of one of the trenches. The main crack surface of this specimen revealed two different crack initiation points 180° from each other, Figure 12 b). The ligament joining those two cracks failed by plastic collapse. As described in the following section, it is postulated that the individual cracks started from trenches. The cross-section inspection revealed that for the 3 and 5 wt.% Ni steels, cracks nucleated at the bottom of

some trenches (Figure 13), reaching a maximum depth of 250 µm and 400 µm, respectively. The specimen with 5 wt.% Ni showed pitting (Figure 14) that could have evolved to a trench in a later stage.

4 DISCUSSION

Trenches were detected on the exposed surface of all the Ni-containing steels after SSRT. ER and RRA were unsuitable ways to assess the nickel effect on trenching. Regardless of the Ni content in the steels, ER showed values between 0.27 and 0.13 and the RRA, between 0.23 and 0.09, with respect to their corresponding values measured in air (Figure 8). The Ni-free steel had the highest ER and RRA values, i.e., 0.27 and 0.23, respectively. Only uniform corrosion was detected on the gauge length. Secondary indications, such as microcracks, were observed adjacent to the main crack. According to the NACE TM0198 standard, the severity of environmentally assisted cracking is assessed on a scale from 1 to 4, with class 4 being the most severe cracking susceptibility. Tests where the loss of ductility is above 20% in respect of the specimens tested in air are classified as Class 3 when no indications of stress corrosion cracking (SCC) are present on the gauge length, and Class 4, if secondary cracks are present on the gauge length and/or signs of SCC are observed on the fracture surface.[45] All Ni-containing specimens were classified as Class 4, and the Ni-free steel as Class 3.

Figures 10 and 11 show that the Ni effect on trenching persisted below the 1 wt.% threshold in the ISO 15156-2 standard. The occurrence of trenches affects the SSC resistance of steels because they act as effective stress concentrators and crack initiators, Figures 12 and 13. The nickel effect on trenches observed in this work cannot be directly extrapolated to other testing methods, solutions, or steel chemistries and microstructures. Other authors detected trenches in LAS without Ni, including AISI 4130, C110 casing steel, and API X65 grades with a tempered martensite microstructure and a YS between 600 and 800 MPa after mechanical tests in a H_2S saturated NACE solution A ($pp H_2S$ = 101.3 kPa).[22–24,34,35,54,55] Therefore, although trenches were exclusively observed in Ni-containing steels in this work, a holistic consideration of reported studies does not warrant a more severe restriction on the Ni concentration for LAS for sour service.

Results shown in this work indicated that tensile stresses are required for the occurrence of trenches, e.g., Figure 4 vs. Figure 10, in accord with previous studies.[22–24,34,35,54,55] It is postulated that the strain applied during the SSRT perturbs the otherwise protective film, favoring the onset of localized corrosion proceeding as trenches in this system. The stress required for the onset of trenching was not measured, but it is postulated that it coincided with the decrease in the potential observed before reaching the yield stress, Figure 9 b). This decrease in potential was a hallmark of OCP curves for all Ni-containing steels measured during SSRT. This sustained decrease in potential persisted up to the point of failure, most likely due to the presence of fresh metal surface exposure resulting from the formation and growth of trenches which favor an increase in the anodic kinetics. The Ni-free steel presented a similar OCP evolution with time with and without applied loads, Figure 9 a). The slight reduction in the measured OCP near the tensile strength is likely the result of an increase in localized plastic strain suffered by the specimens. Localized plastic deformation perturbed the protective film locally and favored the presence of microcracks in the vicinity of the primary fracture, Figure 10 b (left).

In this work, using thiosulfate as a surrogate for H_2S bubbling was validated for carbon steels with Ni content up to 5 wt.% given that the sulfide films were similar to those formed in H_2S-containing solutions[36,51,56–59] and their rupture led to trenches in SSRTs at OCP[22–26,30,31]. These trenches, as discussed later, are like the ones reported by other authors after mechanical testing in H_2S aqueous solutions. [22–26,30,31] The differences in electrochemical behavior and film formation reaction among the steels with different Ni concentration that could explain the difference in SSRT

performance are discussed below. The sequence of damage identified in this work suggests that those differences in electrochemical behavior favor pit formation that evolves to a trench and finally into a crack.

4.1 Effect of Ni on electrochemical behavior

The OCP varied with exposure time, Ni concentration, and the addition of thiosulfate to the NACE TM0177 solution A. For the solution without thiosulfate, the OCP decreased after 72 h of exposure (Figure 2 b). This shift in the active direction could be related to the dissolution of the original oxide formed by air exposure. The OCP measured at the beginning of the experiment increased when thiosulfate was added to the base solution. This increase in OCP is expected considering the addition of a reducible species[60]. The OCP after 72 h in NACE solution A with thiosulfate increased with nickel content (Figure 2 b). XRD diffraction patterns (Figure 5) show cementite and sulfides enriched in the corrosion products layer, both of which have a noble potential vs. the bare steel.[37,51,57–59] The increase in OCP with Ni content is in accordance with the decrease in the kinetics of the anodic reaction and the increase in the rate of the reduction reactions, Figure 6.[60] According to Staehle et al., the oxidation kinetics rate is decreased when the number of sites available for the anodic reaction to occur is reduced, which can be attained by adding more noble alloying elements to the base metal or by the formation of an insoluble corrosion products layer on the metallic surface.[60] The increase in the cathodic kinetics of the charge-transfer controlled reduction reactions can be related to a catalytic effect of nickel on the hydrogen evolution reaction[61,62]. With regards to the increase in the current density with nickel in the diffusion-limited zone after 24 h of exposure at OCP, a possible explanation is the increase in surface area available for cathodic reactions by forming conductive corrosion product layers[57–59].

4.2 Ni influence on the sulfide film

Iron sulfides are good electron conductors and present nobler electrode potentials than iron.[56–59] As the nickel content in the steels increased, the presence of a nickel sulfide, Ni_3S_2, with a rhombohedral crystalline structure (JCPDS/ICDD 01-085-1802) was identified (Figure 5 b), in accordance with previous results.[62–66] Ni_3S_2 is characterized by a bipyramidal arrangement where three nickel atoms form a triangular base and two S atoms occupy the vertices of each pyramid.[67] Nickel bisulfide is also known as heazlewoodite, a mineral found in the earth's crust that consists of an intermetallic stable phase at room temperature with a content of 27 wt.% S, according to the Ni-S phase diagram reported by Okamoto.[68] Sulfides favor the formation of galvanic cells with ferrite, where the sulfides act as preferential cathodic sites.[57–59] Cementite is also an electron conductor that allows the occurrence of cathodic reactions.[69] Rupture of those protective layers by strain during SSRT, even during the elastic strain regime, could have exposed bare metal and favored localized corrosion reactions at the tip of pits and trenches, supported by cathodic reactions that can occur on the filmed surface.

4.3 Pit-to-trench transition

Trench formation is suggested to initiate from hemispherical pits (Figures 4 and 14) on the surface of the specimen when subjected to tensile stress in thiosulfate-containing solutions. While it was postulated that the threshold stress for trench formation is below the yield stress, pits can act as concentrators of the nominal uniaxial stress and contribute to an inhomogeneous distribution of the stress. At the bottom of hemispherical pits, stress can increase up to threefold the nominal values.[70] Eventually, stress values close to or above the yield stress can be reached thus enhancing plastic deformation in the vicinity of the stress concentrator.[71] Consequently, in the presence of tensile stress, bare metal exposure at the tip of pits might favor the onset of localized corrosion reactions required for trench formation. It is worth noting that, in contrast to hemispherical pits, trench morphology consists of elongated deep features that advance perpendicularly to the direction of maximum applied stress.

4.4 Trench-to-crack transition

Based on the current analysis of cross sections and in agreement with other authors [22,25], a higher nickel content increased trench depth (Figure 11) and hence favored a trench-to-crack transition in LAS exposed to H_2S-containing environments at OCP (Figure 13). For the tests conducted in this work, under an increasing tensile stress level, a crack will eventually nucleate at the trench tip (Figures 12 and 13). According to the literature, trench-to-crack is particularly evident when the concentration of H_2S is low (pH_2S < 0.3 kPa) or when it is present at partial pressures ranging from 0.56 kPa to 3.04 kPa.[25] The estimated equivalent partial pressure of H_2S for the thiosulfate-containing solution studied in this work is 0.56 kPa.[39] This finding is also consistent with the observations made by Craig, who reported a transition from trenches to cracks in AISI 4140 quenched and tempered steels with additions of 2 and 4 wt.% Ni when exposed to a constant load at 80% YS in a NACE TM0177 solution A saturated with H_2S at a partial pressure of 101.3 kPa at OCP.[22] However, the dimensions of the observed indications were not quantified by the author.

The parameters obtained from the cross-section inspection were compared with the results reported by Yamane for laboratory steels containing up to 2.18 wt.% Ni in a 0.5 wt.% acetic acid solution at a pH_2S of 3.04 kPa. The average trenches width for the steels studied here was approximately half of those reported by Yamane.[25] The depth of the trenches measured in this work was consistent with those obtained by Yamane. The aspect ratio (d/a) varied by a factor of 2 between the results of the present study and those reported by Yamane. Nonetheless, an increasing trend of the aspect ratio with nickel addition to the steels was observed in both works. The aspect ratio is a good indicator of the sharpness of the secondary indications, and a higher value of d/a represents sharper trenches or cracks.

It is worth noting that the nucleation and growth of trenches may occur even in steels with Ni content below 1 wt.%. Depending on the stress level, type of test (e.g., constant load or displacement, SSRT, etc.), and exposure time, the nucleated trenches may transform into cracks. Therefore, imposing a maximum limit on nickel content based on accelerated laboratory tests may have limited practical implications.

5 CONCLUSIONS

Carbon steels with a Ni content varying between 0 and 5 wt.% with a tempered martensite microstructure and comparable yield strength of 610 MPa and a hardness level below or equal to 22 HRC, were evaluated in NACE TM0177 solution A with sodium thiosulfate as a surrogate for H_2S bubbling with and without applied tensile stress. The role of Ni on SSC initiation was analyzed at OCP. The results presented herein support the following conclusions:

- Ni additions favored the formation of a Ni-containing sulfide, Ni_3S_2. This film retarded the anodic reactions on the surface and enhanced the reduction reaction rates in the thiosulfate acid brines, thus increasing the OCP measured after 72 h of exposure. Regardless of the Ni content, iron sulfides such as pyrrhotite and cubic FeS were also identified after 72 h of exposure at OCP. Nickel and iron sulfides are electron conductors and can act as preferential cathodic reaction sites, favoring steel corrosion.

- Under applied tensile stresses, the main role of nickel content was on the morphology of secondary indications on the gauge length. The Ni-free steel showed uniform corrosion. Trenches were formed in Ni-containing steels, even when the nickel content was below 1 wt.%. The aspect ratio of these trenches increased with the nickel content in the steels. It is not feasible to establish a threshold regarding the nickel

content as per ISO 15156-2 standard. Therefore, enhancing the resistance to trenching when developing nickel-containing steels for service in sulfide environments is crucial.

- The potentials measured after 72 h in NACE TM0177 solution A with thiosulfate were within the H_2S stability field of the Pourbaix diagram of the $S_2O_3^{2-}$-H_2O system at room temperature, and below the potential for the hydrogen evolution reaction. Thus, substituting H_2S bubbling with thiosulfate additions, as proposed by Tsujikawa, is considered acceptable for the studied steels.

6 ACKNOWLEDGMENTS

This work was funded by YPF Tecnología (YTEC), Tenaris (Techint), and the Argentinian Council of Academic Research (CONICET). The authors acknowledge Dr. Raul Rebak (GE) for providing the alloys to conduct this research and Eng. Luis Alberto Aguirre (YTEC) and Dr. Walter Morris (YTEC) for coordinating the project. The technical discussions that were held with Dr. Martin Valdez and Dr. María José Cancio (Tenaris) are greatly appreciated by the authors.

7 REFERENCES

1. Vollmer, L.W., *Corrosion* 8 (1952): pp. 326–332.
2. NACE Technical Practices Committee, “Field Experience with Cracking of High Strength Steels in Sour Gas and Oil Wells”, in Symposium on Sulfide Stress Cracking, ed. NACE (Houston, Texas: NACE, 1952), p. 351–354.
3. J.P. Fraser, and G.G. Eldredge, *Corrosion* 14 (1958): pp. 45–50.
4. J.P. Fraser, and R.S. Treseder, *Corrosion* 8 (1952): pp. 342–350.
5. R.S. Treseder, T.M. Swanson, *Corrosion* 24 (1968): pp. 31–37.
6. TM 0177 “Test Method Laboratory Testing of Metals for Resistance to Sulfide Stress Cracking and Stress Corrosion Cracking in H_2S” (Houston, Texas: NACE International, 2016).
7. MR0175 “Sulfide Stress Cracking Resistant Metallic Materials for Oilfield Equipment” (Houston, Texas: NACE International, 2002).
8. ISO 15156-2: Petroleum and Natural Gas Industries — Materials for Use in H_2S-containing Environments in Oil and Gas Production, Third Edition (Geneva, Switzerland, ISO International, 2015).
9. H. Asahi, Y. Sogo, M. Ueno, and H. Higashiyama, *Corrosion* 45 (1989): pp. 519–527.
10. C. Mendibide, and T. Sourmail, *Corros Sci* 51 (2009): pp. 2878–2884.
11. B. Craig, “Hydrogen Damage,” in ASM Handbook Corrosion: Fundamentals, Testing, and Protection, eds. S.D. Cramer, and B.S.Jr. Covino (ASM International, 2003), pp. 367–380.
12. M. Elboujdaini, “Hydrogen-Induced Cracking and Sulfide Stress Cracking,” in Uhlig’s Corrosion Handbook: Third Edition, Edited by R. Winston Revie (John Wiley & Sons, Inc., 2011), pp. 183–194.
13. T. Perez, *JOM* 65 (2013): pp. 1033–1042.
14. E. Snape, *Corrosion* 24 (1968): pp. 261–282.
15. B.D. Craig, *Corrosion* 38 (1982): pp. 457–463.
16. A.R. Jarvis, and J.H. Bulloch, *International Journal of Pressure Vessels and Piping* 49 (1992): pp. 271–307.
17. M. Iannuzzi, A. Barnoush, and R. Johnsen, *npj Materials Degradation* 1:2 (2017): pp. 1–11.
18. W.T. Becker, and R.J. Shipley, “Hydrogen Damage and Embrittlement,” in ASM Handbook Volume 11: Failure Analysis and Prevention, eds. W.T. Becker, and R.J. Shipley (ASM International, 2002), pp. 809–822.
19. R.A. Grange, *Metallurgical Transactions* 4 (1973): pp. 2231–2244.

20. L. Norström, and O. Vingsbo, *Metal Science* 13 (1979): pp. 677–684.
21. M. Kappes, M. Iannuzzi, R.B. Rebak, and R.M. Carranza, *Corrosion Reviews* 32 (2014): pp. 101–128.
22. B.D. Craig, J.K. Brownlee, and T. V. Bruno, *Corrosion* 48 (1992): pp. 90–96.
23. Y. Yoshino, and Y. Minozaki, *Corrosion* 42 (1986): pp. 222–233.
24. J.H. Payer, S.P. Pednekar, and W.K. Boyd, *Metallurgical Transactions A* 17 (1986): pp. 1601–1610.
25. Y. Yamane, N. Totsuka, M. Kimura, T. Kurisu, K. Motoda, and Y. Nakai, "Effect of Ni on Sulfide Stress Corrosion Cracking in Low Alloy Steels," in Corrosion 86 (Houston, Texas: March 17-21, 1986), paper 167.
26. A.K. Dunlop, *Corrosion* 34 (1978): pp. 88–96.
27. A. Ikeda, T. Kaneko, and Y. Ando, *Corros Sci* 27 (1987): pp. 1099–1115.
28. T. Kaneko, and A. Ikeda, *Transactions ISIJ* 28 (1988): pp. 575–577.
29. H. Husby, P. Wagstaff, M. Iannuzzi, R. Johnsen, and M. Kappes, *Corrosion* 74 (2018): pp. 801–818.
30. B.D. Craig, J.K. Brownlee, and T. V Bruno, *Corrosion* 46 (1990): pp. 142–146.
31. H. Asahi, and M. Ueno, *ISIJ International* 34 (1994): pp. 290–294.
32. D.L. Sponseller, *Corrosion* 48 (1992): pp. 159–171.
33. J.G. Erlings, H.W. de Groot, and J. Nauta, *Corros Sci* 27 (1987): pp. 1153–1167.
34. C. Mendibide, and C. Duret-Thual, *Corrosion* 77 (2021): pp. 433–444.
35. I. Samusawa, D. Izumi, and J. Shimamura, *Materials and Corrosion* (2021): pp. 1–9.
36. S. Tsujikawa, A. Miyasaka, M. Ueda, S. Ando, T. Shibata, T. Haruna, M. Katahira, Y. Yamane, T. Aoki, and T. Yamada, *Corrosion* 49 (1993): pp. 409–419.
37. M. Kappes, G.S. Frankel, N. Sridhar, and R.M. Carranza, *Corrosion* 68 (2012): pp. 872–884.
38. M.A. Kappes, "Evaluation of Thiosulfate as a Substitute for Hydrogen Sulfide in Sour Corrosion Fatigue Studies", (The Ohio State University, 2011).
39. M.A. Kappes, M.A., G.S. Frankel, N. Sridhar, and R.M. Carranza, *J Electrochem Soc* 159 (2012): pp. C195–C204.
40. S. Parodi, M. Kappes, J.L. Otegui, R. Carranza, and A. Aguirre, *Matéria* 23 (2018).
41. M.J. Peet, "Bainitic Steels and Alloys for Power Plants," in Structural Alloys for Power Plants; Operational Challenges and High-Temperature Materials, Eds. A. Shirzadi, and S. Jackson, (Woodhead Publishing, 2014), pp. 153–187.
42. K. Krog, and A.H. Qvale, "Low Alloy Steels for Large Bore Subsea Connectors," Robuste materialvalg i oljeindustrien (2012).
43. ASTM E112, "Standard Test Methods for Determining Average Grain Size", (ASTM International, 1996).
44. ASTM G1-03 "Standard Practice for Preparing, Cleaning, and Evaluating Corrosion Test", (ASTM International, 1999).
45. TM0198 "Slow Strain Rate Test Method for Screening Corrosion-Resistant Alloys (CRAs) for Stress Corrosion Cracking in Sour Oilfield Service", (NACE International, 2016).
46. C.D. Kim, and B.E. Wilde, "A Review of the Constant Strain Rate Corrosion Cracking Test," in Stress Corrosion Cracking–The Slow Strain-Rate Technique, Eds. G. Ugiansky, and J. Pyer (ASTM International, 1979), pp. 97–112.
47. ASTM G129 "Standard Practice for Slow Strain Rate Testing to Evaluate the Susceptibility of Metallic Materials to Environmentally Assisted Cracking", (ASTM International, 2000).
48. J. Crank, The Mathematics of Diffusion (Clarendon Press, Oxford, 1975).
49. D.R. Chalfoun, M.A. Kappes, P. Bruzzoni, and M. Iannuzzi, *Int J Hydrogen Energy* 47 (2022): pp. 3141–3156.
50. G. Renaud, *Surf Sci Rep* 32 (1998): pp. 5–90.
51. D. Rickard, "Metastable Sedimentary Iron Sulfides," in Sulfidic Sediments and Sedimentary Rocks, Ed. D. Rickard (2012), pp. 195–231.
52. Y. Liu, Z. Zhang, N. Bhandari, Z. Dai, F. Yan, G. Ruan, A.Y. Lu, G. Deng, F. Zhang, H. Al-Saiari, A.T. Kan, and M.B. Tomson, *Ind Eng Chem Res* 56 (2017): pp. 9016–9027.
53. "High-Strength Structural and High-Strength Low-Alloy Steels," in ASM Handbook Vol.1: Irons, Steels and High-Performance Alloys (ASM International, 1990), pp. 389–423

54. J.A. Colwell, J.H. Payer, and W.K. Boyd, "Performance of Steels in High Pressure Environments Containing Low H_2S Concentrations," in Corrosion 86 (Houston, Texas, NACE International, 1986), paper 168.
55. T. Anderson, W. Huang, G. Wadsworth, H.J. Jun, D. Fairchild, T. Neeraj, and A. Ozekcin, "Micrographic Acceptance Criteria for SSC Testing," in Corrosion 2020 (2020), paper C2020-14845.
56. D.W. Shoesmith, P. Taylor, M.G. Bailey, and D.G. Owen, *J Electrochem Soc* 127 (1980): pp. 1007–1015.
57. J.S. Smith, and J.D.A. Miller, *British Corrosion Journal* 10 (1975): pp. 136–143.
58. R.A. King, J.D.A. Miller, and J.S. Smith, *British Corrosion Journal* 8 (1973): pp. 137–141.
59. J. Kvarekvål, and J. Moloney, "Sour Corrosion," in Trends in Oil and Gas Corrosion Research and Technologies: Production and Transmission (Elsevier Ltd., 2017), pp. 113–147.
60. R.W. Staehle, J.J. Royuela, T.L. Raredon, E. Serrate, C.R. Morin, and R.V. Farrar, *Corrosion* 26 (1970): pp. 451–486.
61. B.E. Wilde, C.D. Kim, and J.C. Turn, *Corrosion* 38 (1982): pp. 515–524.
62. Y. Wang, F. Jin, X. Zeng, C. Ma, F. Wang, G. Yao, and Z. Jing, *Appl Energy* 104 (2013): pp. 306–309.
63. J.B. Parise, *Acta Crystallogr B* 36 (1980): pp. 1179–1180.
64. Y.U. Jeong, and A. Manthiram, *Inorg Chem* 40 (2001): pp. 73–77.
65. A. D'Aloya, G. Senanayake, D. Ralph, and A. Nikoloski, *Hydrometallurgy* 183 (2019): pp. 45–50.
66. J.T. Ho, and G.P. Yu, *Corrosion* 48 (1992): pp. 145–153.
67. P.A. Metcalf, B.C. Crooker, M. McElfresh, Z. Kakol, and J.M. Honig, *Phys Rev B* 50 (1994): pp. 2055–2060.
68. H. Okamoto, *J Phase Equilibria Diffus* 30 (2009): pp. 123–123.
69. J.L. Crolet, N. Thevenot, and S. Nesic, "Role of Conductive Corrosion Products on the Protectiveness of Corrosion Layers," in Corrosion 96 (Denver, 1996), paper 4.
70. J. Schijve, *Fatigue of Structures and Materials* (Springer, 2009).
71. G.E. Dieter, *Mechanical Metallurgy* (McGraw-Hill, 1988).
72. T. Hemmingsen, *Electrochim Acta* 37 (1992): pp. 2775–2784.

8 FIGURE CAPTIONS

Figure 1. Microstructure of a) carbon steel without nickel, b) 1 wt.% Ni-containing steel c) 5 wt.% Ni-containing steel

Figure 2. a) OCP evolution in steels with 0, 0.5, 1, 3, and 5 wt.% Ni during 72 h of exposure in a deaerated NACE solution A substituted with 10^{-3} M $S_2O_3^{2-}$. Duplicated tests are shown, data was acquired every one second and is presented as scatter points joined by a line for better visualization. b) Open circuit potentials at the beginning of the test (black symbols) and after 72 hours (gray symbols) in the NACE solution A (filled symbols) and the one substituted with thiosulfate (empty symbols). The lines were added to aid the visualization of the trends.

Figure 3. $S_2O_3^{2-}$ - H_2O Pourbaix diagram at 298 K and 101.3 kPa assuming 10^{-3} M for all the dissolved species. The OCP values obtained after 72 h of exposure in the surrogated NACE solution A were included for all the alloys studied. Note that the potentials are reported in the normal hydrogen electrode (NHE) scale. The numbers indicated on each equilibrium line correspond to the reactions detailed in Appendix 1.

Figure 4. Appearance of the sulfide film formed on the specimens' surface of a) 0 wt.% Ni, b) 1 wt.% Ni, c) 5 wt.% Ni steels, and the corresponding corrosion morphology observed after cleansing in inhibited HCl of d) 0 wt.% Ni, e) 1 wt.% Ni, f) 5 wt.% Ni steels.

Figure 5. Grazing XRD patterns for steels a) 0 wt.% Ni, and b) 5 wt.% Ni, after 72 h of exposure at OCP (above) and as-ground to 600 grit (below).

Figure 6. a) Anodic and b) Cathodic potentiodynamic polarization curves in a deaerated NACE solution A substituted with 10^{-3} M $S_2O_3^{2-}$ for all the steels studied.

Figure 7. Stress-strain curves obtained in air (dashed lines) and in 10^{-3} M $S_2O_3^{2-}$ substituted NACE solution A at OCP (solid lines).

Figure 8. Effect of Ni on the ductility loss calculated as RE (left-axis) and RRA (right-axis) after SSRT.

Figure 9. OCP evolution vs. time in presence and absence of applied loads, OCP_{SSRT} and OCP_{72h}, respectively for a) 0 wt.% Ni steel, b) 1 wt.% Ni steel, and c) 3 wt.% Ni steel.

Figure 10. Appearance of the gauge length after a) and b) SEM examination, c) optical microscopy inspection, for all the steels studied.

Figure 11. Trench/crack a) Density (#indications/mm), b) mean depth (µm), c) mean width (µm), and d) aspect ratio (d/a) versus Ni content.

Figure 12. 0.5 wt.% Ni steel a) Close-up of a trench, and b) cracking surface after SSRT at OCP.

Figure 13. Details of cracks nucleated at the bottom of a trench in a) 3 wt.% Ni steel, and b) 5 wt.% Ni steel, after SSRT at OCP.

Figure 14. 5 wt.% Ni steel a) Pits nucleated close to the gauge length to the shoulder radii transition, b) elongated pits on the gauge length, c) details of the elongated pits that promoted trench formation.

9 TABLES

Table 1
Chemical composition and mechanical properties of the steels

Alloy	Chemical Composition [wt.%]							Mechanical Properties				Metallurgic Properties
	C	Mn	Si	Ni	Fe	S (ppm)	P (ppm)	Hardness [HRC]	$R_{p\ 0.2\%}$ [MPa, (ksi)]	Plastic Elongation	Reduction in Area [%]	Average PAGS [µm]
0	0.16	1.24	0.25	--	Bal.	8.9	4.4	< 20	604 (88)	0.227 ± 0.009	86.0 ± 2.1	33.0
0.5	0.17	1.22	0.25	0.48	Bal.	8.9	6.4	< 20	614 (89)	0.242 ± 0.011	86.4 ± 1.0	24.3
1	0.16	1.22	0.25	0.97	Bal.	7.7	4.5	21	609 (88)	0.227 ± 0.006	83.0 ± 0.6	20.2
3	0.16	1.32	0.22	3.06	Bal.	8.6	5.6	21	630 (91)	0.240 ± 0.002	78.9 ± 5.8	25.5
5	0.16	1.31	0.24	5.04	Bal.	8.8	6.3	20	608 (88)	0.259 ± 0.002	84.8 ± 0.9	19.6

10 APPENDIX 1

The open circuit potentials measured after 72 h in NACE TM0177 solution A substituted with 10^{-3} M $S_2O_3^{2-}$ were located in the Pourbaix diagram of Figure 3, which was constructed according to the reactions reported in the literature for $S_2O_3^{2-}$-containing aqueous solutions.[72] The reactions are detailed below, and calculations for the equilibrium lines of the Pourbaix diagram were conducted considering a concentration of 10^{-3} M for all the dissolved species, HS_2O^{3-}, $S_2O_3^{2-}$, and H_2S, at a temperature of 298 K and 101.3 kPa of pressure.

$$1)\ HS_2O_3^- + 5H^+ + 4e^- \leftrightarrow 2S + 3H_2O \qquad E_0 = 0.440\ V_{ENH}$$

$$2)\ S_2O_3^{2-} + 6H^+ + 4e^- \leftrightarrow 2S + 3H_2O \qquad E_0 = 0.465\ V_{ENH}$$

$$3)\ S_2O_3^{2-} + 10H^+ + 8e^- \leftrightarrow 2H_2S + 3H_2O \qquad E_0 = 0.303\ V_{ENH}$$

4) $S + 2H^+ + 2e^- \leftrightarrow H_2S$ $E_0 = 0.142\ V_{ENH}$

5) $S_2O_3^{2-} + 8H^+ + 8e^- \leftrightarrow 2HS^- + 3H_2O$ $E_0 = 0.200\ V_{ENH}$

6) $HS_2O_3^- \leftrightarrow S_2O_3^{2-} + H^+$ $pK_{a2} = 1.69$

7) $H_2S \leftrightarrow HS^- + H^+$ $pK_{a1} = 7.02$

Figures PAPER CORROSION JOURNAL PART I

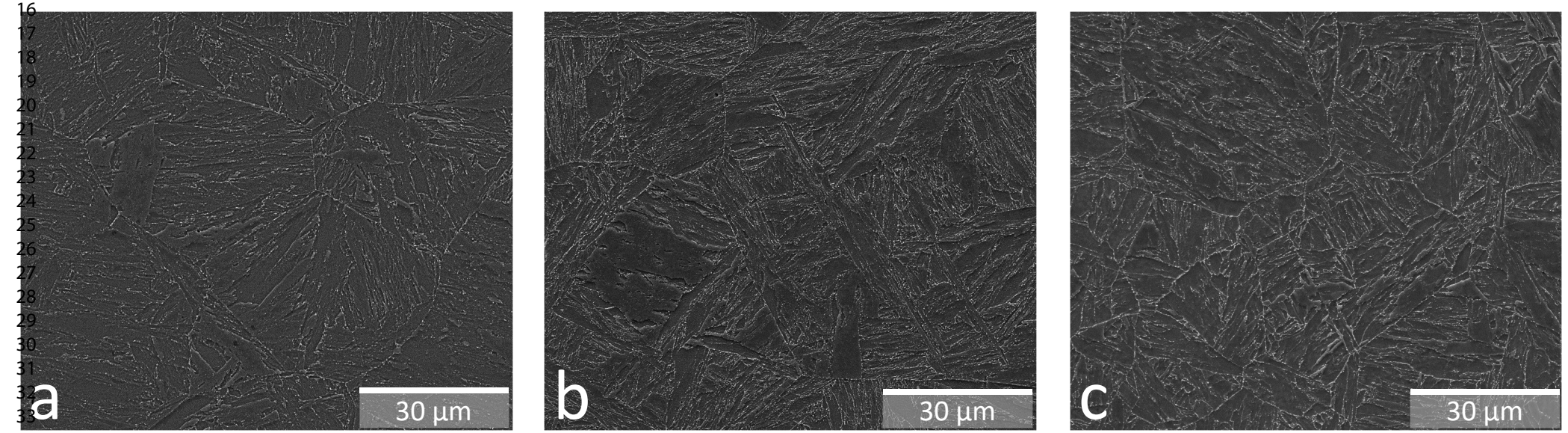

Figure 1. Microstructure of a) carbon steel without nickel, b) 1 wt.% Ni-containing steel c) 5 wt.% Ni-containing steel

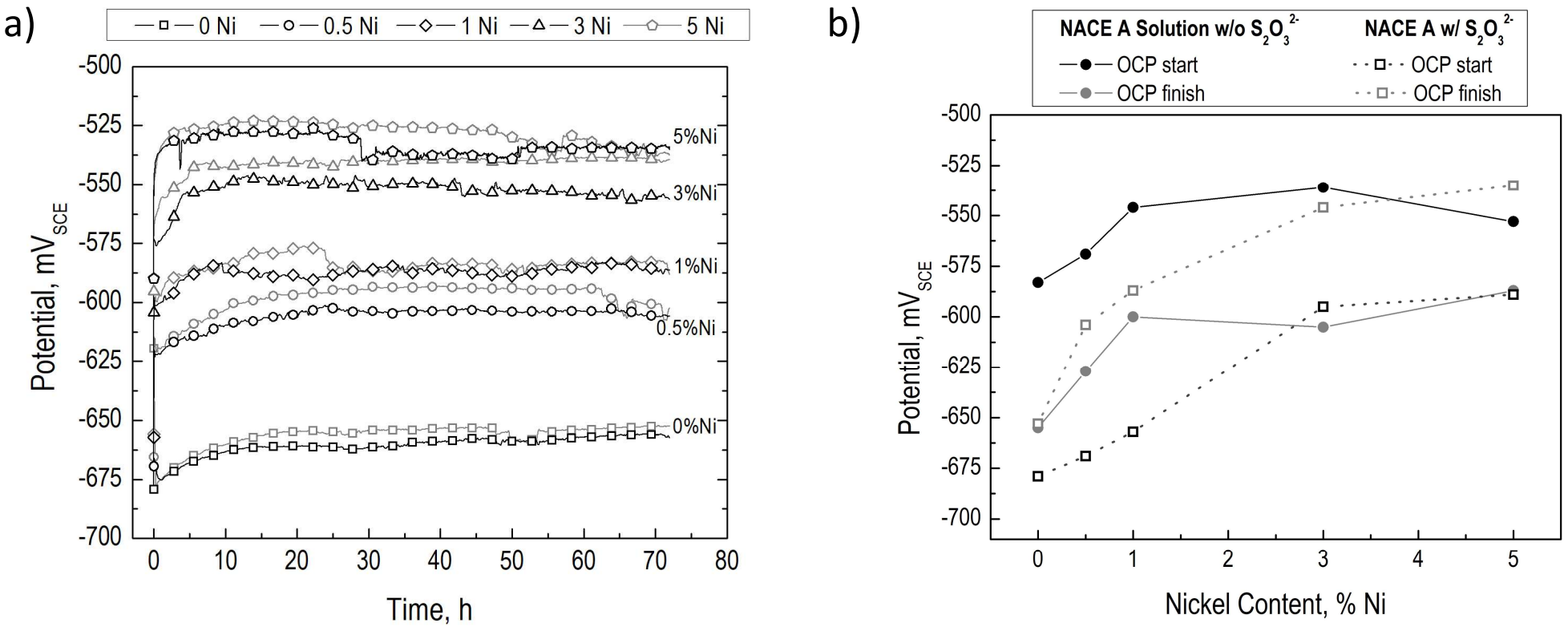

Figure 2. a) OCP evolution in steels with 0, 0.5, 1, 3, and 5 wt.% Ni during 72 h of exposure in a deaerated NACE solution A substituted with 10^{-3} M $S_2O_3^{2-}$. Duplicated tests are shown, data was acquired every one second and is presented as scatter points joined by a line for better visualization. b) Open circuit potentials at the beginning of the test (black symbols) and after 72 hours (gray symbols) in the NACE solution A (filled symbols) and the one substituted with thiosulfate (empty symbols). The lines were added to aid the visualization of the trends.

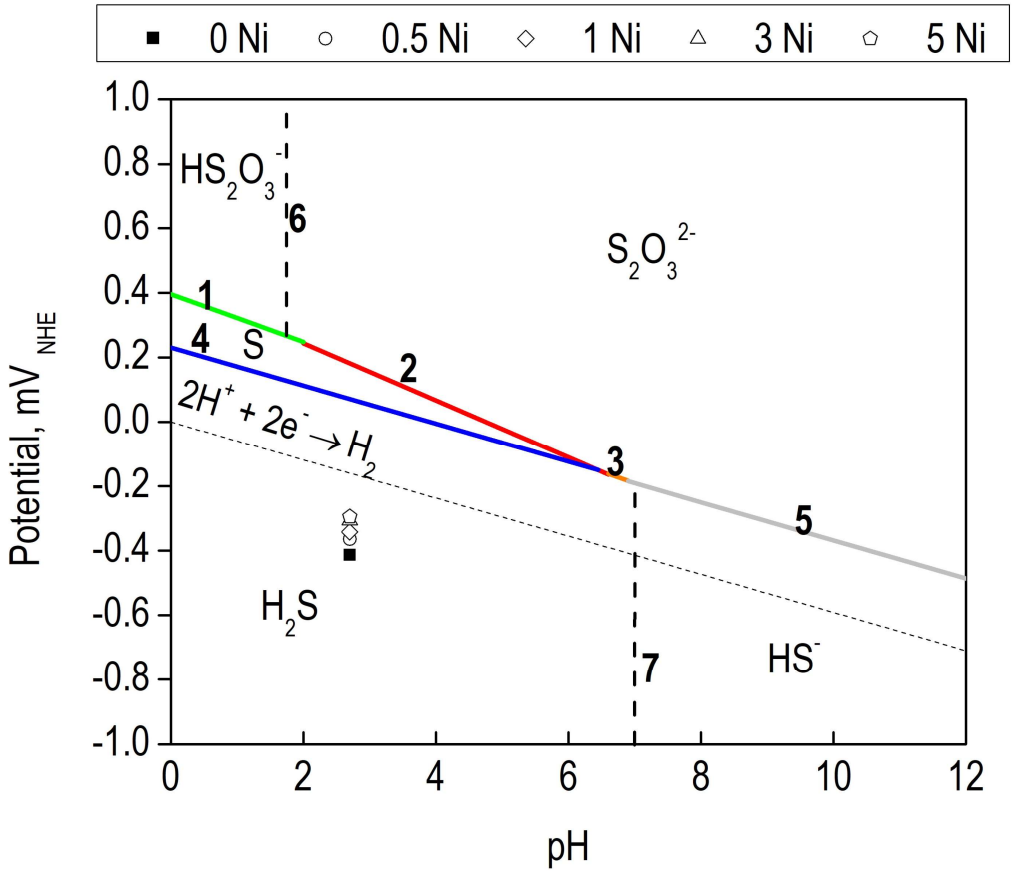

Figure 3. $S_2O_3^{2-}$ - H_2O Pourbaix diagram at 298 K and 101.3 kPa assuming 10^{-3} M for all the dissolved species. The OCP values obtained after 72 h of exposure in the surrogated NACE solution A were included for all the alloys studied. Note that the potentials are reported in the normal hydrogen electrode (NHE) scale. The numbers indicated on each equilibrium line correspond to the reactions detailed in Appendix 1.

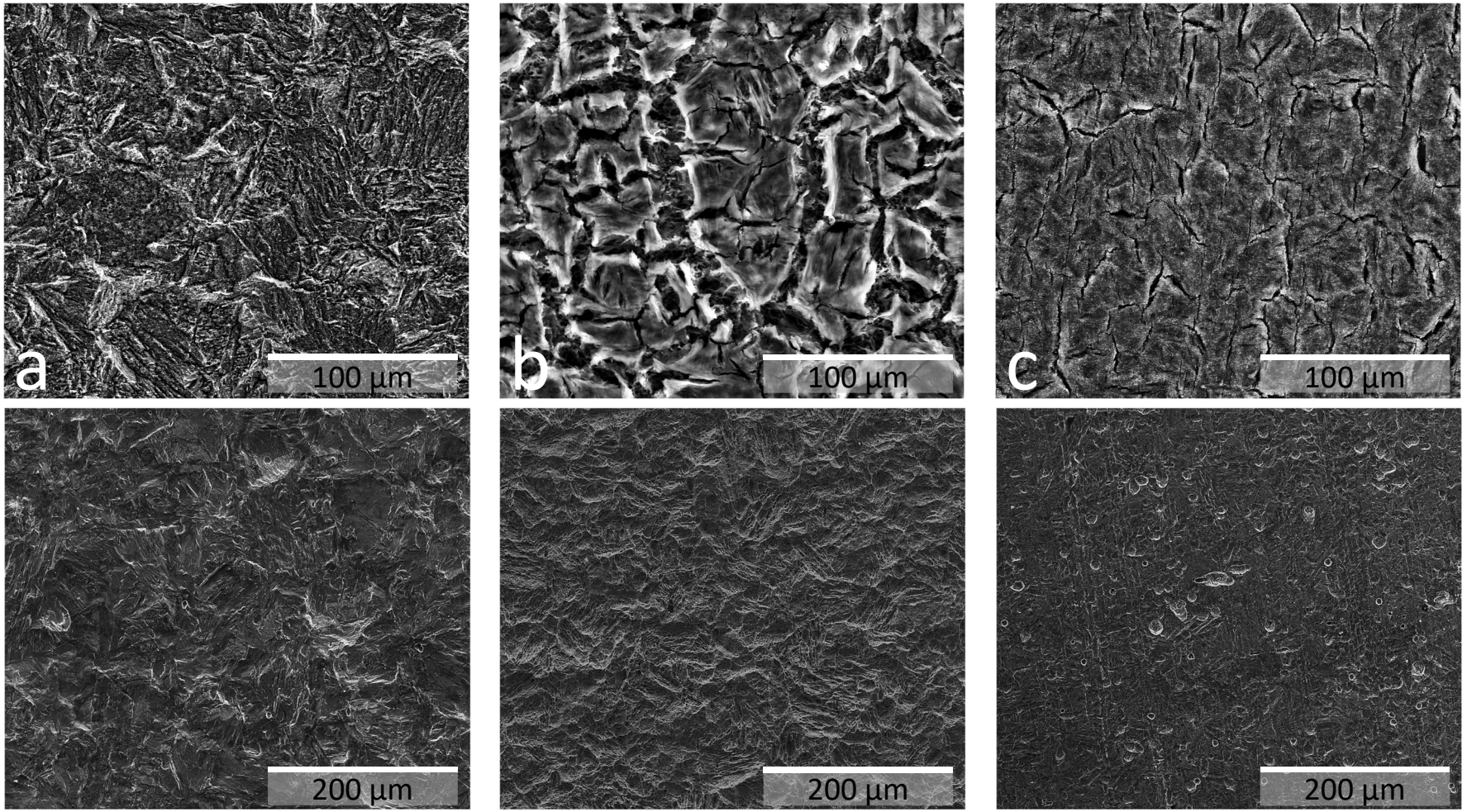

Figure 4. Appearance of the sulfide film formed on the specimens' surface of a) 0 wt.% Ni, b) 1 wt.% Ni, c) 5 wt.% Ni steels, and the corresponding corrosion morphology observed after cleansing in inhibited HCl of d) 0 wt.% Ni, e) 1 wt.% Ni, f) 5 wt.% Ni steels.

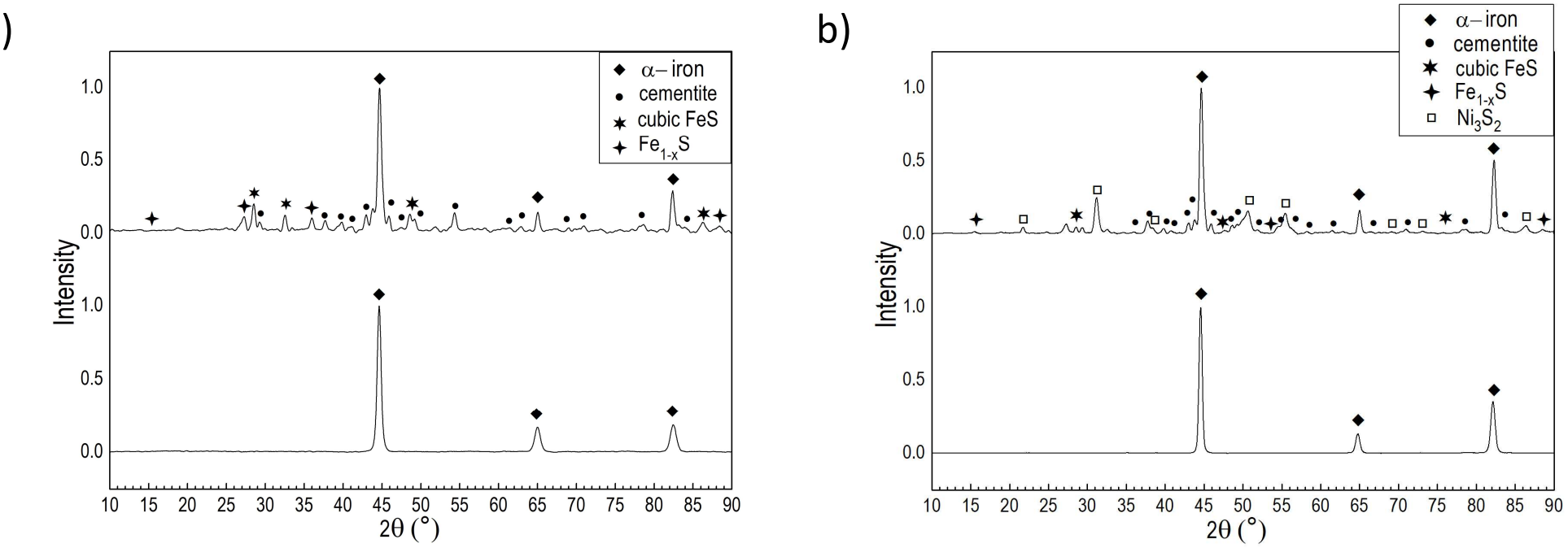

Figure 5. Grazing XRD patterns for steels a) 0 wt.% Ni, and b) 5 wt.% Ni, after 72 h of exposure at OCP (above) and as-ground to 600 grit (below).

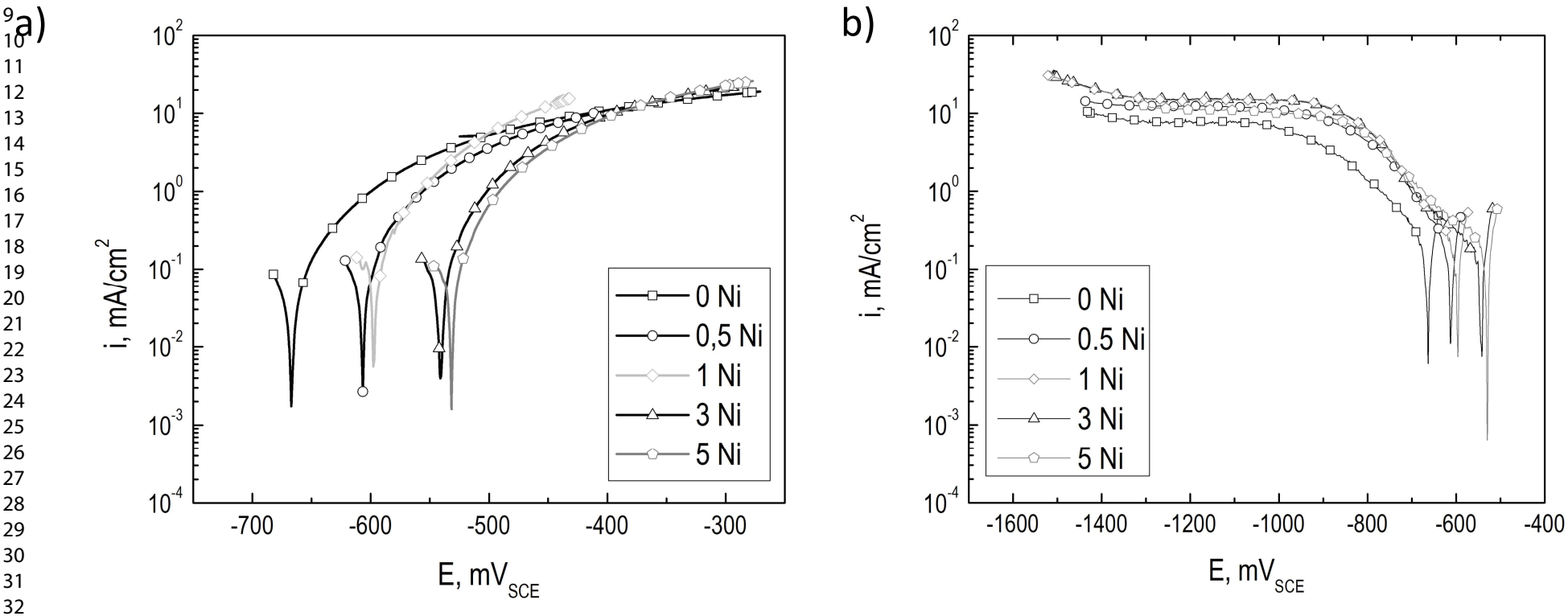

Figure 6. a) Anodic and b) Cathodic potentiodynamic polarization curves in a deaerated NACE solution A substituted with 10^{-3} M $S_2O_3^{2-}$ for all the steels studied.

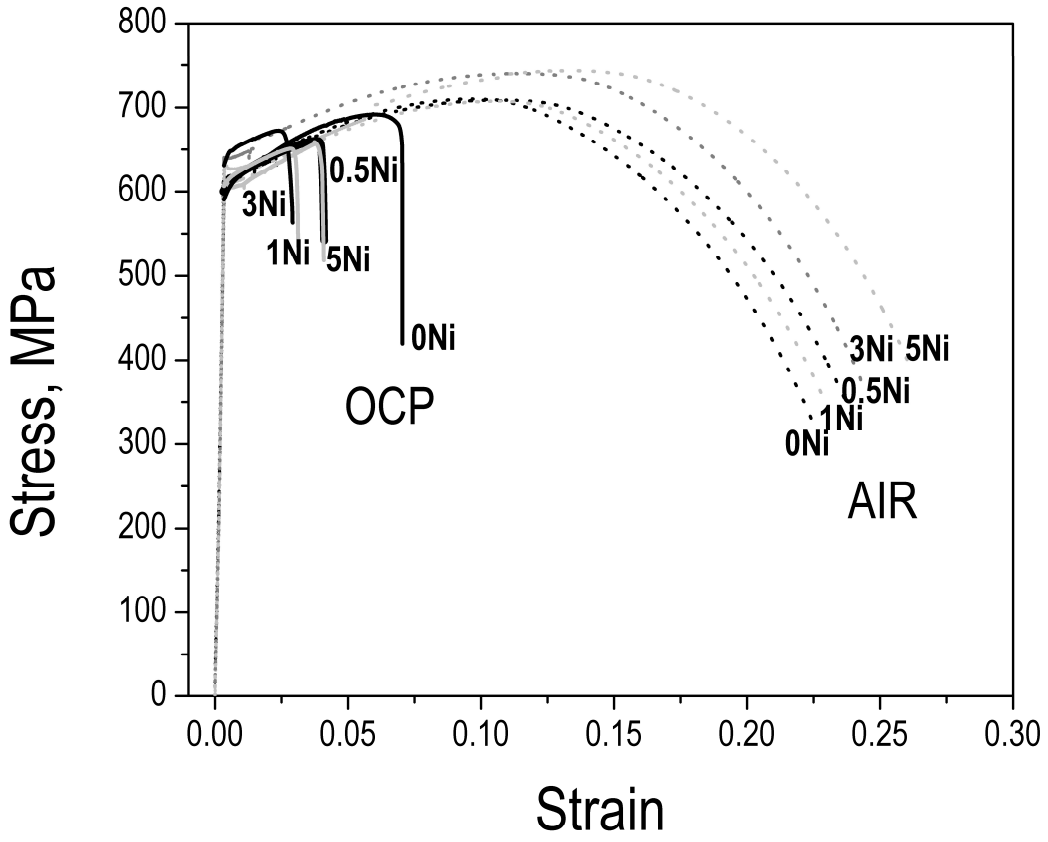

Figure 7. Stress-strain curves obtained in air (dashed lines) and in 10^{-3} M $S_2O_3^{2-}$ substituted NACE solution A at OCP (solid lines).

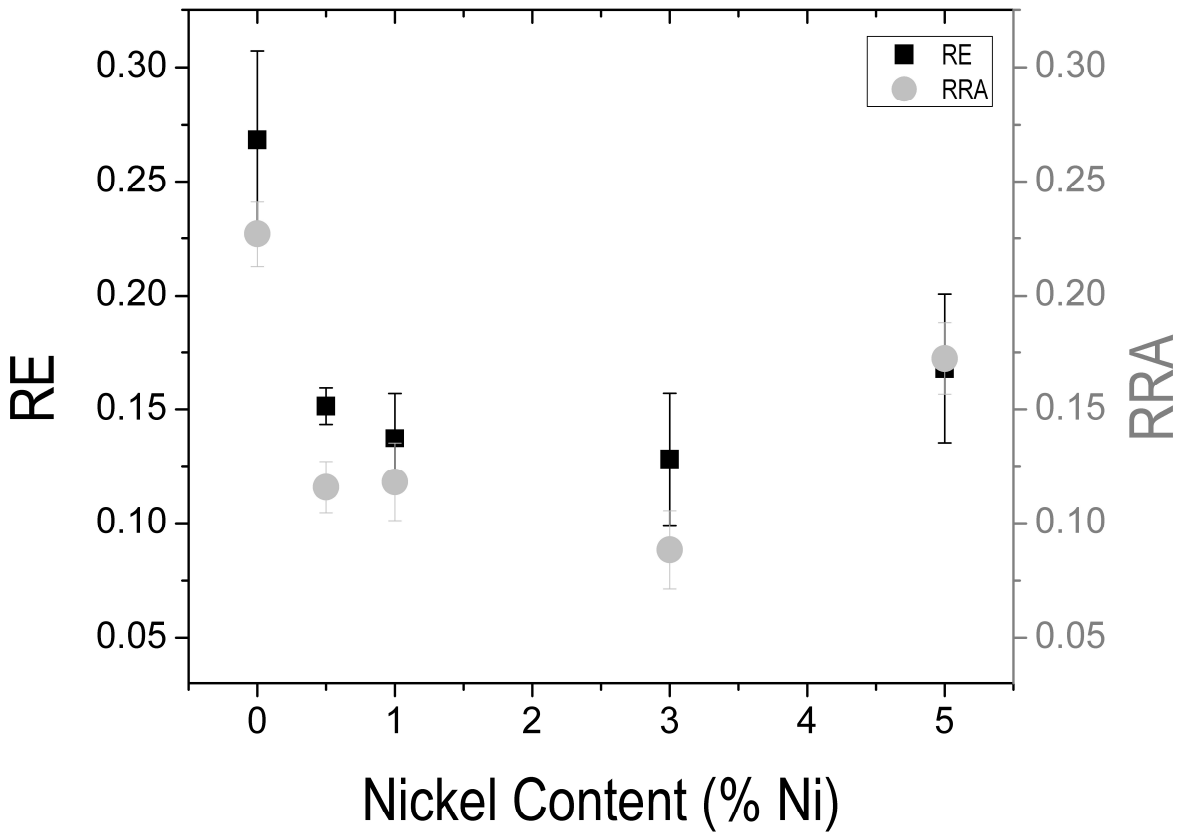

Figure 8. Effect of Ni on the ductility loss calculated as RE (left-axis) and RRA (right-axis) after SSRT.

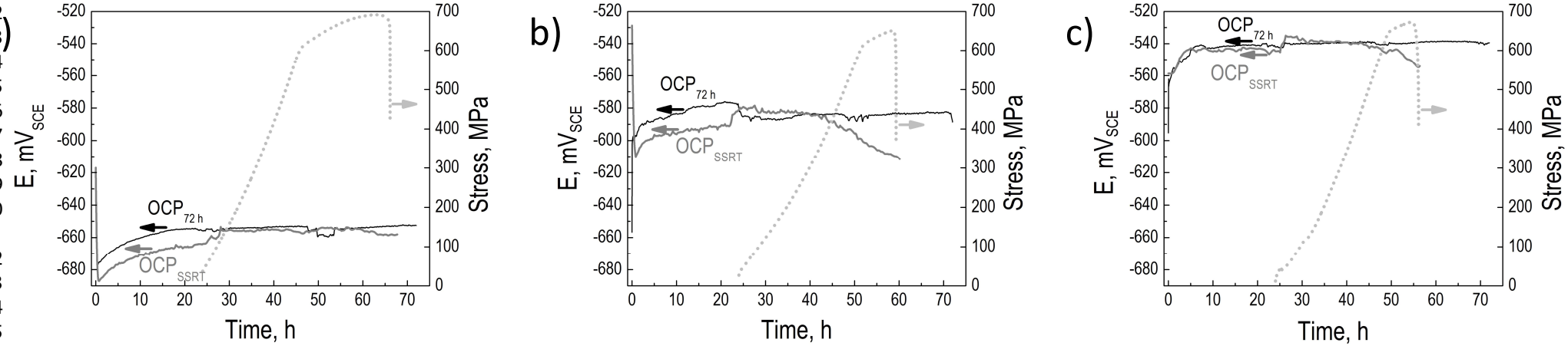

Figure 9. OCP evolution vs. time in presence and absence of applied loads, OCP_{SSRT} and OCP_{72h}, respectively for a) 0 wt.% Ni steel, b) 1 wt.% Ni steel, and c) 3 wt.% Ni steel.

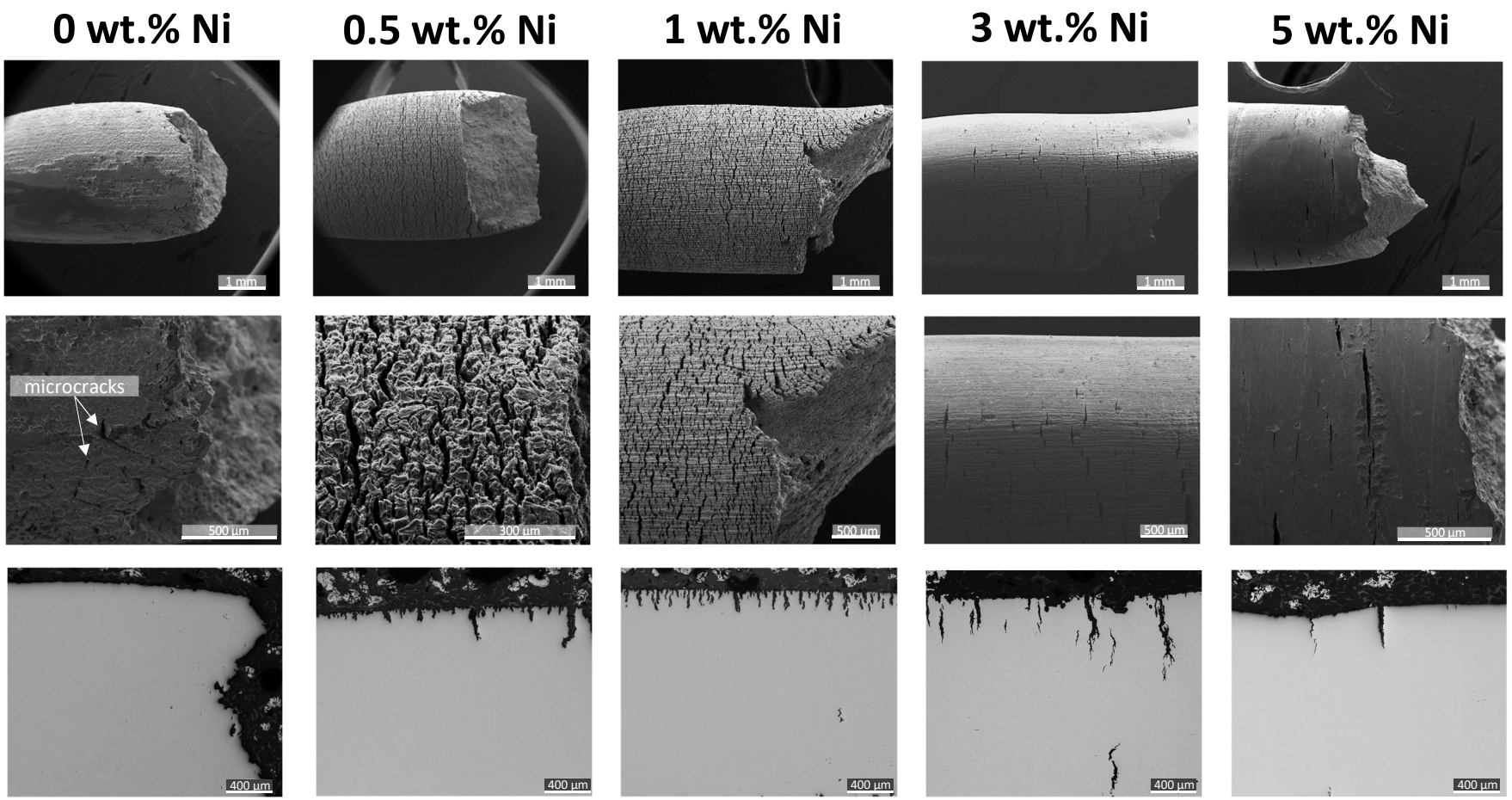

Figure 10. Appearance of the gauge length after a) and b) SEM examination, c) optical microscopy inspection, for all the steels studied.

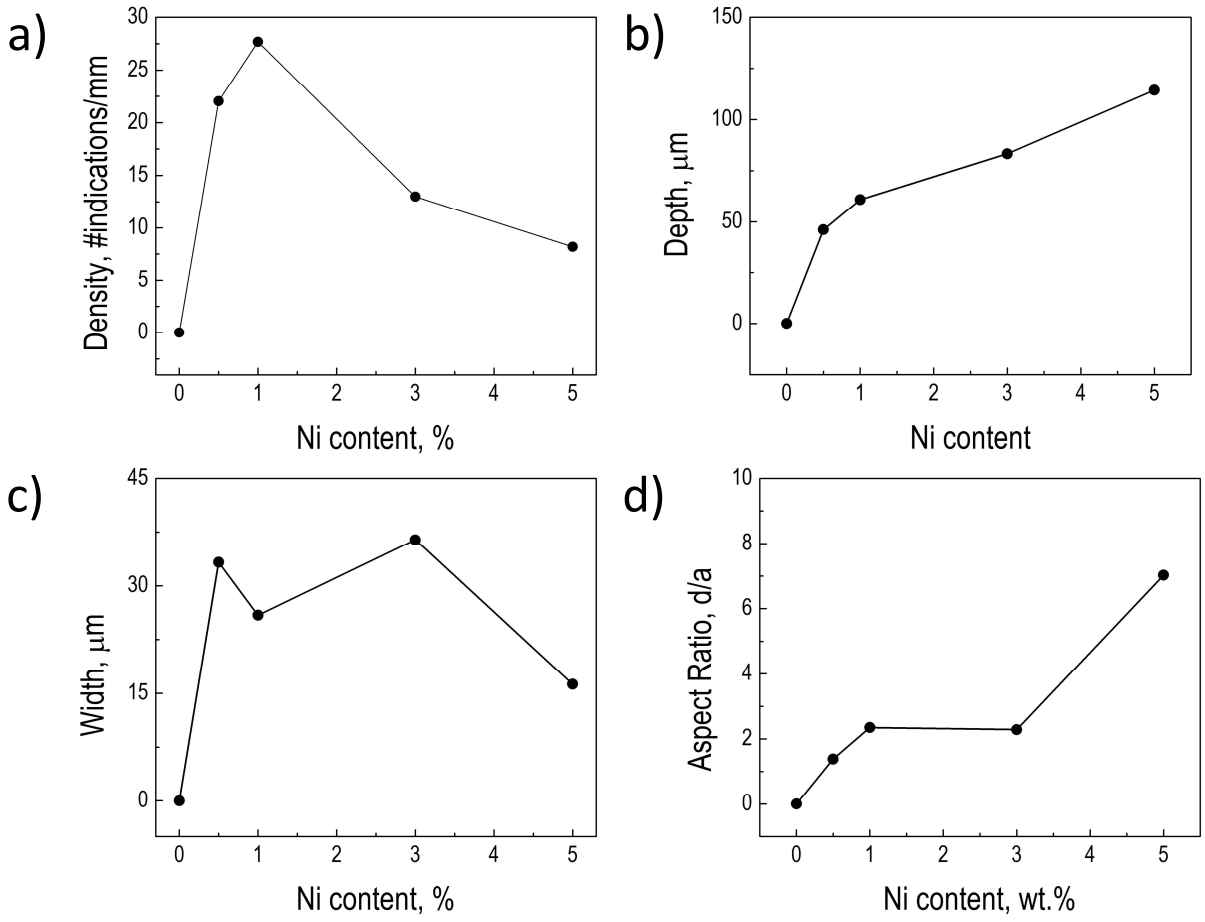

Figure 11. Trench/crack a) Density (#indications/mm), b) mean depth (µm), c) mean width (µm), and d) aspect ratio (d/a) versus Ni content.

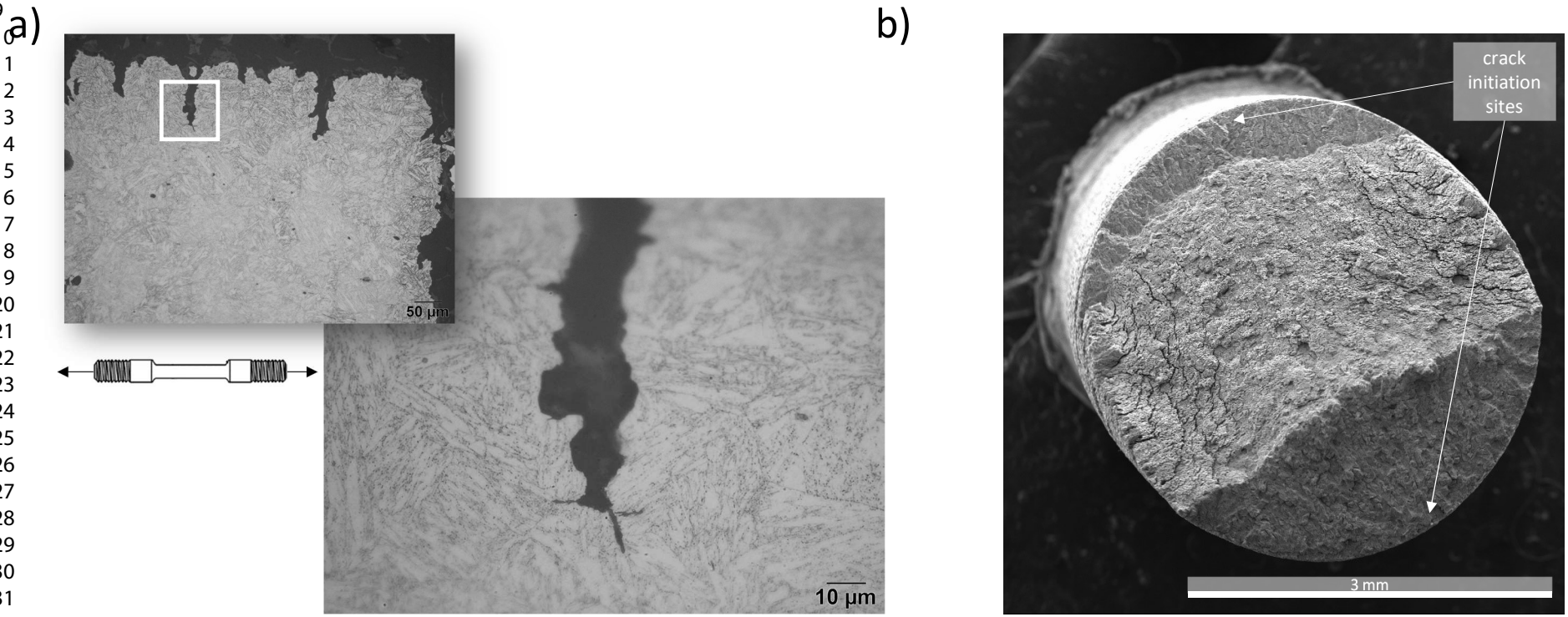

Figure 12. 0.5 wt.% Ni steel a) Close-up of a trench, and b) cracking surface after SSRT at OCP.

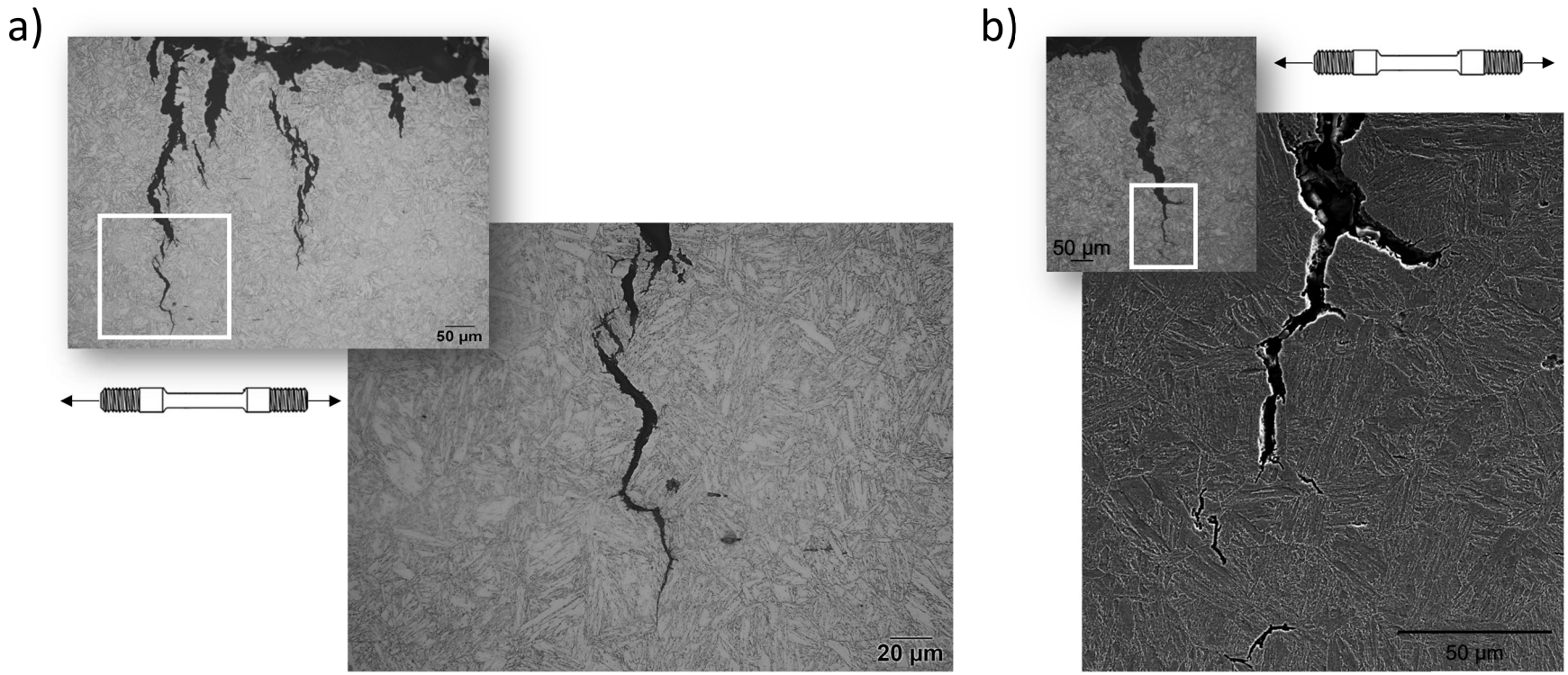

Figure 13. Details of cracks nucleated at the bottom of a trench in a) 3 wt.% Ni steel, and b) 5 wt.% Ni steel, after SSRT at OCP.

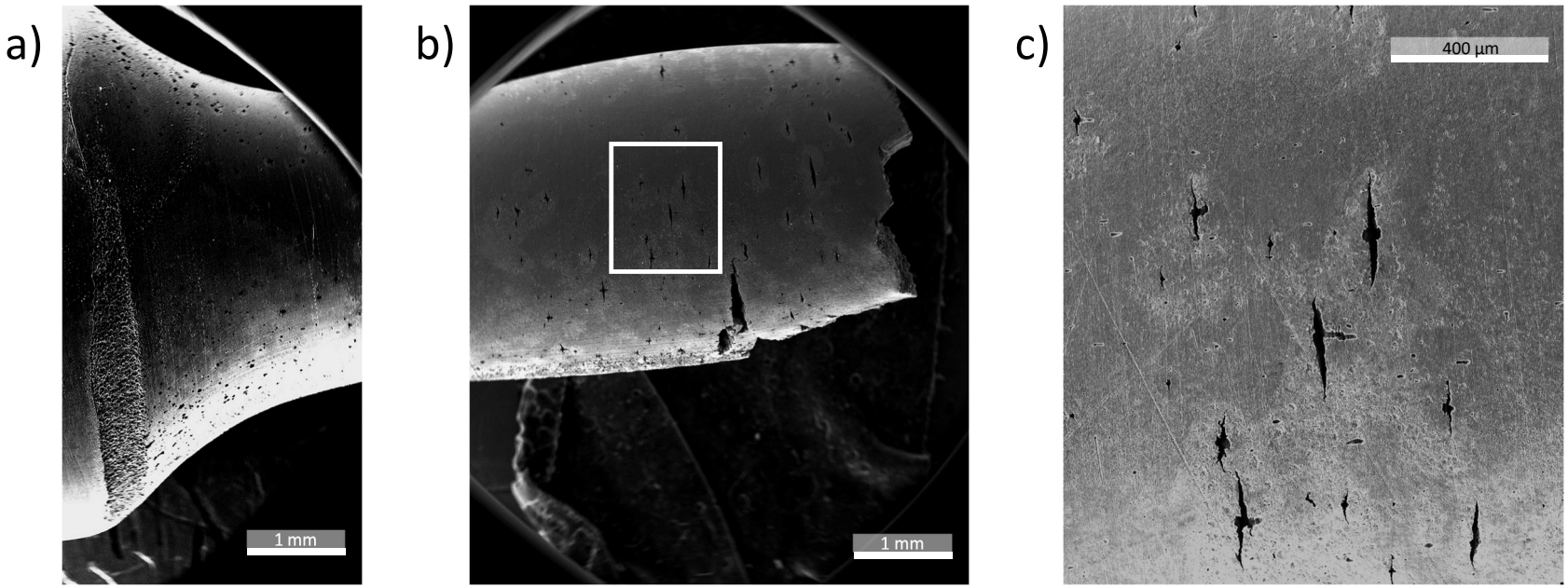

Figure 14. 5 wt.% Ni steel a) Pits nucleated close to the gauge length to the shoulder radii transition, b) elongated pits on the gauge length, c) details of the elongated pits that promoted trench formation.